Prkar1a is an osteosarcoma tumor suppressor that defines a molecular subclass in mice

Sam D. Molyneux,[1] Marco A. Di Grappa,[1] Alexander G. Beristain,[1] Trevor D. McKee,[1] Daniel H. Wai,[2] Jana Paderova,[1] Meenakshi Kashyap,[1] Pingzhao Hu,[3] Tamara Maiuri,[1] Swami R. Narala,[1] Vuk Stambolic,[1] Jeremy Squire,[1] Josef Penninger,[4] Otto Sanchez,[1] Timothy J. Triche,[2] Geoffrey A. Wood,[1] Lawrence S. Kirschner,[5] and Rama Khokha[1]

[1]Ontario Cancer Institute, Toronto, Ontario, Canada. [2]Childrens Hospital Los Angeles, Los Angeles, California, USA. [3]Centre for Applied Genomics, The Hospital for Sick Children, Toronto, Ontario, Canada. [4]Institute of Molecular Biotechnology, Vienna, Austria. [5]Department of Molecular Virology, Immunology and Medical Genetics, Human Cancer Genetics Program, The Ohio State University, Columbus, Ohio, USA.

Some cancers have been stratified into subclasses based on their unique involvement of specific signaling pathways. The mapping of human cancer genomes is revealing a vast number of somatic alterations; however, the identification of clinically relevant molecular tumor subclasses and their respective driver genes presents challenges. This information is key to developing more targeted and personalized cancer therapies. Here, we generate a new mouse model of genomically unstable osteosarcoma (OSA) that phenocopies the human disease. Integrative oncogenomics pinpointed cAMP-dependent protein kinase type I, α regulatory subunit (*Prkar1a*) gene deletions at 11qE1 as a recurrent genetic trait for a molecularly distinct subclass of mouse OSA featuring RANKL overexpression. Using mouse genetics, we established that *Prkar1a* is a bone tumor suppressor gene capable of directing subclass development and driving RANKL overexpression during OSA tumorigenesis. Finally, we uncovered evidence for a *PRKAR1A*-low subset of human OSA with distinct clinical behavior. Thus, tumor subclasses develop in mice and can potentially provide information toward the molecular stratification of human cancers.

Introduction

Common mutational processes underpin the development of diverse cancers by perturbing key regulatory networks that have evolved to resist the emergence of neoplastic cells in normal tissues. Some human cancers have been stratified into subclasses that vary in their clinical behavior due to the unique engagement of specific pathways (1–3). A compendium of somatic alterations is being compiled by cancer genome mapping projects (4–7); however, identifying clinically relevant molecular tumor subtypes and their corresponding driver genes presents challenges. Elucidating pathways that underlie the emergence of these subclasses will yield therapeutic targets for customized cancer treatment.

Modeling human cancers in the mouse has been accomplished using transgenics as well as through conditional and regulatable gene targeting; a growing body of evidence shows that mice recapitulate the fundamental aspects of human cancer (8). Whether mice also spontaneously develop molecular tumor subclasses is less explored. Mouse models have been matched to subclasses within human histopathological groups (9, 10) and can mimic drug responses of patients, when bearing pathogenetically relevant mutations (1). Genomic instability is a ubiquitous feature of human tumors, and models that recapitulate this have been exploited for cancer gene discovery (11, 12). Tumor subpopulations arising in mice could similarly provide vital insights for the stratification of cognate human tumors as well as a means to assess the directive capacity of specific gene alterations in spontaneous subclass development.

Osteosarcoma (OSA) is the second highest cause of cancer-related death in the pediatric age group (13). Despite modern surgery and systemic chemotherapy, survival rates are low, with approximately 35% of patients dying within 5 years of diagnosis (14). Originating from cells of the osteoblast lineage, OSA tumors exhibit complex, unbalanced karyotypes, characterized by numerous recurrent DNA amplifications and deletions as well as gross chromosomal abnormalities (15). Individuals with heterozygous germline mutations of *TP53* or *RB1* have a far greater propensity to develop OSA (16), and allelic loss of these genes is found in a high proportion of sporadic OSA tumors (17). The loss of $p16^{INK4A}$ and $p14^{ARF}$ expression through INK4A deletion or amplification of *MDM2* and *CDK4* at 12q13 occurs in other patients (18, 19), indicating that functionally equivalent alterations in the p53/Rb pathways are a near obligate feature of OSA. Indeed, mice bearing the combined conditional deletion of p53 and pRb in preosteoblasts or p53 in committed osteoblasts develop spontaneous OSA at high frequency (20–22). Loss of p53, but not Rb alone, was sufficient to promote tumorigenesis, whereas the loss of both exhibited strong synergy. Other alterations in human OSA include high expression of *MYC*, *MET*, and *FOS* (23, 24); transgenic *FOS* expression in mice results in bone sarcomas, some of which are osteogenic (25, 26). Overall, the prevalence of widespread copy number alterations (CNAs) in OSA point to the existence of many unidentified OSA genes.

Here, we apply mouse genetics and oncogenomics to a model, which we believe is new, of genomically unstable OSA to identify potential driver genes and their relationship with OSA heterogeneity. We pinpoint *Prkar1a* as a bone tumor suppressor, the loss of which deregulates PKA signaling and induces RANKL overexpression. *Prkar1a* deletion defines a molecular subclass in mice, and we subsequently uncover initial evidence for a parallel subclass in human OSA that displays low *PRKAR1A* expression and clinically distinct behavior (referred to herein as *PRKAR1A*-low).

Authorship note: Sam D. Molyneux and Marco A. Di Grappa contributed equally to this work.

Conflict of interest: The authors have declared that no conflict of interest exists.

Citation for this article: *J Clin Invest.* 2010;120(9):3310–3325. doi:10.1172/JCI42391.

Results

A transgenic mouse model of human OSA. To generate tumorigenesis in the bone we cloned SV40 T/t antigen (TAg) under control of the murine osteocalcin promoter, which is specific for mature osteoblasts (OG2; Figure 1A) (27). The large T antigen oncoprotein binds and inactivates p53 and pRb (28), while the small t targets the tumor suppressor PP2A (29). Three Murine Osteocalcin TAg OSA (MOTO) transgenic lines were established from independent FVB founders and displayed varying transgene copy numbers (Supplemental Figure 1A; supplemental material available online with this article; doi:10.1172/JCI42391DS1). Using FISH, transgene insertion was mapped to chromosome 12qA-B1 for the MOTO-1 line (Figure 1A and Supplemental Figure 1C). TAg RNA showed bone-specific expression (Figure 1B); the protein was observed in 11- to 15-week-old bones (Supplemental Figure 1B) and localized to osteoblasts (Figure 1C). MOTO mice developed normally and formed multi-ostotic bone tumors with complete penetrance. Mice developed tumors at a young age and became morbid after 21 weeks of age (Figure 1D). The MOTO-3 line also displayed prostate tumors (data not shown) and was thus excluded. MOTO-1 and MOTO-2 mice ($n > 350$) exhibited skeletal tumors at all sites known to be affected in the human disease, with a peak incidence in the long bones as is seen in human OSA (Figure 1E), although with a higher prevalence of craniofacial tumors. Bone tumors with varying levels of calcification were clearly distinguishable by radiography and CT (Figure 1, F and G, and gross images in Figure 2, A–D). Histology revealed a spectrum of osteoblastic lesions from benign osteoma to aggressive metastatic OSA, with the majority being osteoblastic OSA, with features typical of high-grade–type osteosarcoma (Figure 2, E–I, and detailed in Supplemental Figure 2, A–D). Spontaneous metastases were present in the lungs of more than 90% of mice at the time of morbidity and appeared less frequently in the liver and occasionally in the kidney or spleen (Figure 2, J–Q, and Supplemental Table 1). The lung is frequently targeted by metastasis in human OSA, with the liver being affected much more rarely. The osteoid content of these secondary tumors demonstrated their osteoblastic origin (Figure 2, K, M, and Q). A series of cell lines (moto1.1, moto1.2, moto1.3, and moto2.1) were derived from primary tumors, and their expression of osteoblastic markers was consistent with that found in human OSA cell lines (Supplemental Figure 3, A–C, and ref. 30). TAg coimmunoprecipitated with p53 and Rb1 in moto cell lines (Supplemental Figure 3D) and with p53 in MOTO-1 and MOTO-2 femurs (data not shown). Altogether, MOTO closely approximates human OSA in pubertal onset, skeletal distribution, and radiographic and histologic features as well as in the development of lung metastases. The MOTO model thus adds a valuable resource for the study of this cancer.

Genomically unstable MOTO OSAs exhibit recurrent PKA subunit gene CNAs. We examined whether MOTO OSAs develop genomic instability. Spectral karyotype (SKY) analysis of MOTO tumors and cell lines revealed high levels of aneuploidy. Numerical and structural chromosomal aberrations were found in all samples as clonal and nonclonal, nonrecurrent alterations (Figure 3A), and included nonrecurrent unbalanced translocations (Figure 3B). Two samples were found to be near tetraploid, a state observed in human OSA (Supplemental Figure 4). Next, we analyzed DNA copy number changes using high resolution array comparative genomic hybridization (aCGH; 19.3 KB overall median probe spacing; 14 end-stage long and flat bone tumors, 3 moto cell lines). Genomic imbalances were detected in all samples, with gains and losses ranging from segmental to focal, along with microamplifications and deletions (<100 KB). The frequency of CNAs along each chromosome was calculated, revealing numerous recurrent events in MOTO OSA (Figure 3C).

Somatic CNAs that arise in cancer can mediate rate limiting steps in tumorigenesis through the activation of oncogenes and the loss of tumor suppressors. Within the set of high frequency losses, a focal deletion at 11qE1 (~1.14 Mb) occurred in approximately 38% of primary tumors (Figure 3D, top, and Supplemental Figure 5). This locus contains *Rgs9*, *Gna13*, *9930022D16Rik*, *X83328*, *Slc16a6*, *Arsg*, *Wipi1*, *Prkar1a*, *BC029169*, *Abc8b*, *Abc8a*, *Abca9*, and *Abca6* (Figure 3D, middle). To search for a candidate gene at 11qE1 that might confer selective advantage when deleted during tumor development, sample-matched aCGH and expression profiles were integrated. RNA was prepared from 13 out of 14 tumors, 3 out of 3 cells lines, and normal bones ($n = 3$) for analysis by microarray. Matching aCGH and expression profiles showed that the 13 genes within this region were often concurrently underexpressed compared with normal bone (Figure 3D, bottom). A genomic interval (chromosome 11, 109.42–109.48 Mb) located within the peak region of deletion was identified by minimal common region analysis ($P < 0.001$ and Supplemental Table 2) and was found to singularly contain *Prkar1a*. This gene was consistently underexpressed in 11qE1 deleted samples and displayed the strongest correlation between expression and copy number among the 13 genes ($r = 0.69$, $P < 0.01$; Figure 3D, bottom). Based on these data, we selected *Prkar1a* as the candidate OSA driver gene for the recurrent deletion at 11qE1.

Prkar1a encodes the regulatory 1α (RIα) subunit of the PKA holoenzyme, a heterotetramer of 2 regulatory and 2 catalytic subunits (RIα, RIIα, RIβ, RIIβ, Cα, Cβ, Cγ), which is activated following cAMP binding to the regulatory subunits (31).We reasoned that deletion of other regulatory subunit or amplification of catalytic subunit genes may exert similar effects on PKA signaling in OSA (i.e., pathway deregulation). Searching for CNAs containing these revealed 1 tumor bearing a microamplification (~70 Kb) at 8qC3 (chromosome 8, 86.81–86.88 Mb), which harbored *Prkaca*, *Asf1b*, and a segment of *Lphn1* (Figure 3E, middle). *Prkaca* RNA was overexpressed in this tumor and its expression correlated with copy number across the tumor cohort ($r = 0.74$, $P = 0.001$; Figure 3E, bottom). Interestingly, this sample did not possess deletions at 11qE1. Together, the group of tumors with *Prkar1a* or *Prkaca* CNAs were prospectively designated as PKA^+. For subsequent studies, we chose to focus on the *Prkar1a* gene, due to its higher prevalence of alteration in MOTO OSA compared with that of *Prkaca*.

Prkar1a deletion defines a subclass of mouse OSA and mediates RANKL overexpression. We performed a blinded histological examination of PKA^+ and PKA^- tumors (6 out of 13 PKA^+ tumors, 7 out of 13 PKA^- tumors). Both groups ranged from relatively well-differentiated osteoblastic OSA to fibroblastic poorly differentiated OSA with scant osteoid (Figure 4A and Supplemental Figure 2, E–H), rendering them indistinguishable at this level. PKA is ubiquitously expressed in eukaryotes, and its ability to phosphorylate a large number of serine/threonine targets underscores its pleiotropic effects (31); in osteoblasts, PKA regulates bone turnover as a mediator of parathyroid hormone (PTH) signaling (32). To determine whether PKA subunit gene deletion/amplification transcriptionally impacts pathways involved in bone biology, a gene set was compiled encompassing regulators and effectors in cAMP/PKA signaling and skeletal physiology (837 genes; Supplemental

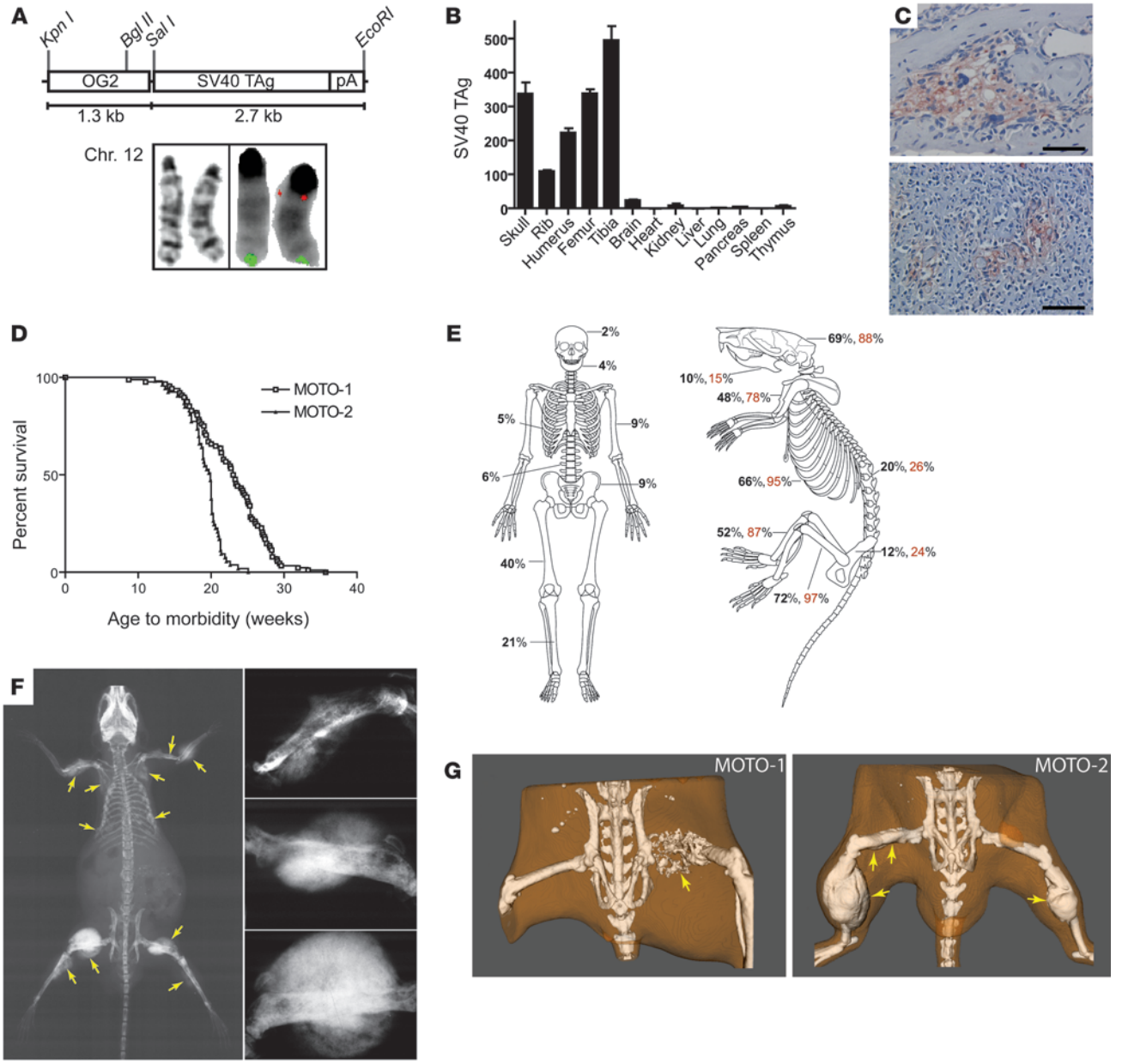

Figure 1

Generation of a transgenic mouse model of OSA. (**A**) The OG2-TAg transgene construct used to generate 3 MOTO founders and FISH mapping of the OG2-TAg construct to chromosome 12qA-B1 in the MOTO-1 line (red indicates the transgene probe; green indicates the control chromosome 12qF2 probe). In the schematic for the transgene construct, "pA" represents a polyadenylation sequence. (**B**) qPCR measurement of SV40 TAg RNA in the tissues of the MOTO-1 mouse (11 weeks old) normalized to 18S; data are represented as mean ± SEM. (**C**) TAg immunostaining shows osteoblast specificity in (top) MOTO-1 rib and (bottom) MOTO-2 femur tumors. Scale bars: 50 μm. (**D**) Kaplan-Meier plot of age to morbidity for MOTO-1 (n = 97) and MOTO-2 mice (n = 91). (**E**) Frequency of OSAs in the human skeleton (adapted with permission from refs. 64 and 65) and the percentage of MOTO-1 (black) and MOTO-2 (red) mice that have at least 1 lesion in the indicated bone. (**F**) Whole-body x-ray images of a 20-week-old MOTO-2 mouse show multiple calcified radiodense tumors in humeri, scapulae, radius/ulna, ribs, femurs, and tibia (arrows). Images on the right show tumors from humerus and both femurs at higher magnification. (**G**) CT images of 18-week-old mice with bone tumors (arrows) show various levels of calcification and bone destruction. A poorly calcified femur tumor (left panel, arrow) and multiple calcified femur and tibia tumors (right panel, arrows) are shown. The small abdominal radiodensities represent intestinal food.

Table 3). An unsupervised analysis using this gene set segregated MOTO tumors into 2 distinct classes, defined by their PKA CNA status (Figure 4B). Interestingly, the *Prkaca*-amplified tumor clustered with those containing *Prkar1a* loss. We compared each of the tumor groups to normal bone (Supplemental Table 4; 5% FDR), and the expression profiles of the 2 classes were found to be enriched for the cAMP/PKA/skeletal gene set (110 genes, PKA^- tumors; 225 genes, PKA^+ tumors; $P < 0.05$). Further, 3-way overlay

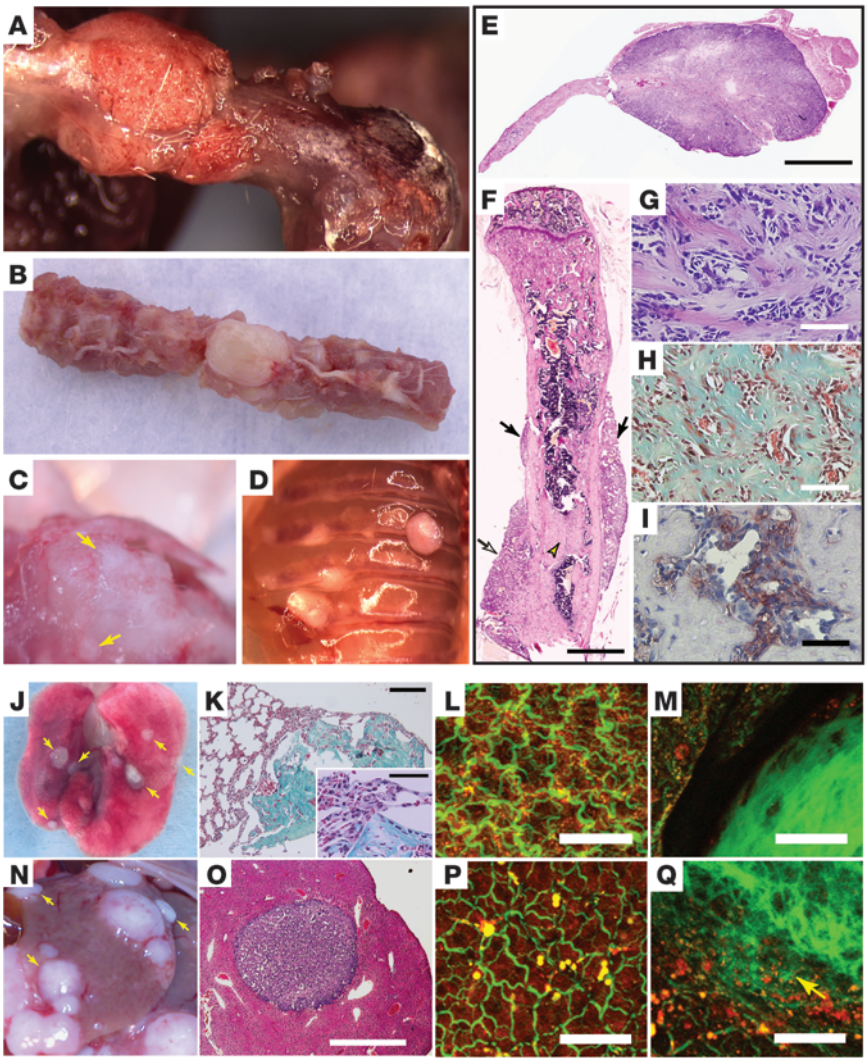

Figure 2
Characterization of OSA in MOTO mice. Gross images of tumors in (**A**) femur, (**B**) spine, (**C**) skull (arrows), and (**D**) ribs. (**E**–**I**) Paraffin sections of osteoblastic tumors: (**E**) Aggressive skull tumor with cortical destruction (stained with H&E), (**F**) humerus with parosteal tumors (arrows) with lesions that are continuous with cortex (open arrow) or within the medulla (open arrowhead) (stained with H&E), (**G**) tumor with cellular atypia (stained with H&E), and (**H**) Masson's trichrome–stained collagen-rich osteoid. (**I**) Alkaline phosphatase staining shows osteoblast specificity. Spontaneous OSA metastases: (**J**, **K**, and **M**) Lung metastases are approximately 1–2 mm, disc shaped, and superficial, (**N**, **O**, and **Q**) while liver metastases are up to 8 mm, spherical, and (**O**) embedded deeper in the parenchyma (stained with H&E). (**K**) Masson's trichrome–stained collagen shows the osteoblastic nature of metastases. (**M** and **Q**) The prominent disorganized collagen in the metastases can be visualized by the second harmonic signal that it generates (green). The red signal is autofluorescence of cellular proteins. (**L**) WT lung and (**P**) liver are shown for comparison. Scale bars: 1 mm (**E**, **F**, and **O**); 150 μm (**K**); 50 μm (**G**–**I**, **K**, inset, **L**, **M**, **P**, and **Q**).

analysis showed the majority of these genes (161 out of 225) to be uniquely overexpressed or underexpressed by PKA$^+$ tumors (Figure 4C). Thus, 2 histopathologically similar but molecularly distinct subclasses of OSA arise in this genetically defined mouse model.

Of the 161 cAMP/PKA/skeletal genes (98 upregulated and 63 downregulated; Supplemental Table 4) that showed altered expression only in MOTO PKA$^+$ tumors, RANKL (*Tnfsf11*) was one of the most highly overexpressed (>17 fold). RANKL is overexpressed in human, cat, and dog OSA (33), and its interference inhibits the growth of rodent OSA cell lines in an orthotopic model (34, 35). Additionally, RANKL is known to be functionally important for metastasis to bone (36). In skeletal biology, a PTH-PKA-RANKL/osteoprotegerin (PTH-PKA-RANKL/OPG) axis operates in osteoblasts, in which stimulation of PTHR1/2 by PTH/PTHrP induces cAMP production (37), activating PKA signaling and altering the transcription of RANKL and OPG through the transcription factor CREB (38). Using quantitative real-time PCR (qPCR), RANKL was found to be invariably overexpressed and OPG was found to often be underexpressed in PKA$^+$ tumors (Figure 4D). We next examined the functionality of this pathway in OSA cells lacking *Prkar1a*. At the RNA level, the moto1.2 cell line underexpressed *Prkar1a*; this was confirmed by Western blot, which showed an absence of RIα protein in these cells (Figure 4E) and a comparable level of Cα to that of 7F2-OSB cells. This loss of RIα was accompanied by a strong baseline elevation of phospho-CREB and high levels of RANKL expression and low levels of OPG expression compared with those of moto1.1 or the osteoblastic control 7F2 cells (Figure 4F) that expressed RIα. Modulation of PKA activity using small molecules showed CREB phosphorylation to be induced by cAMP or forskolin/IBMX treatment, with the latter being reduced when combined with the PKA inhibitor H89 in moto1.2 cells. CREB activation by cAMP stimulated RANKL transcription and suppressed OPG (Figure 4, G and H); H89 cotreatment inhibited RANKL induction. This confirmed the relationship between PKA signaling and RANKL/OPG expression via CREB in OSA cells as is seen in normal osteoblasts. Moreover, loss of RIα protein associated with a high baseline level of phospho-CREB and an abnormal RANKL/OPG ratio in MOTO OSA cells.

Prkar1a is an OSA tumor suppressor gene in mice. We sought to decisively test the impact of *Prkar1a* on OSA using mouse genetics. *Prkar1a*-null mice are embryonic lethal (39); to engineer conditional loss of this gene during OSA tumorigenesis, we bred MOTO-1 mice with *Prkar1a*$^{fl/fl}$ and α1(I)-collagen [Colα1(I)] promoter-Cre recombinase transgenics. The Colα(I)Cre transgene

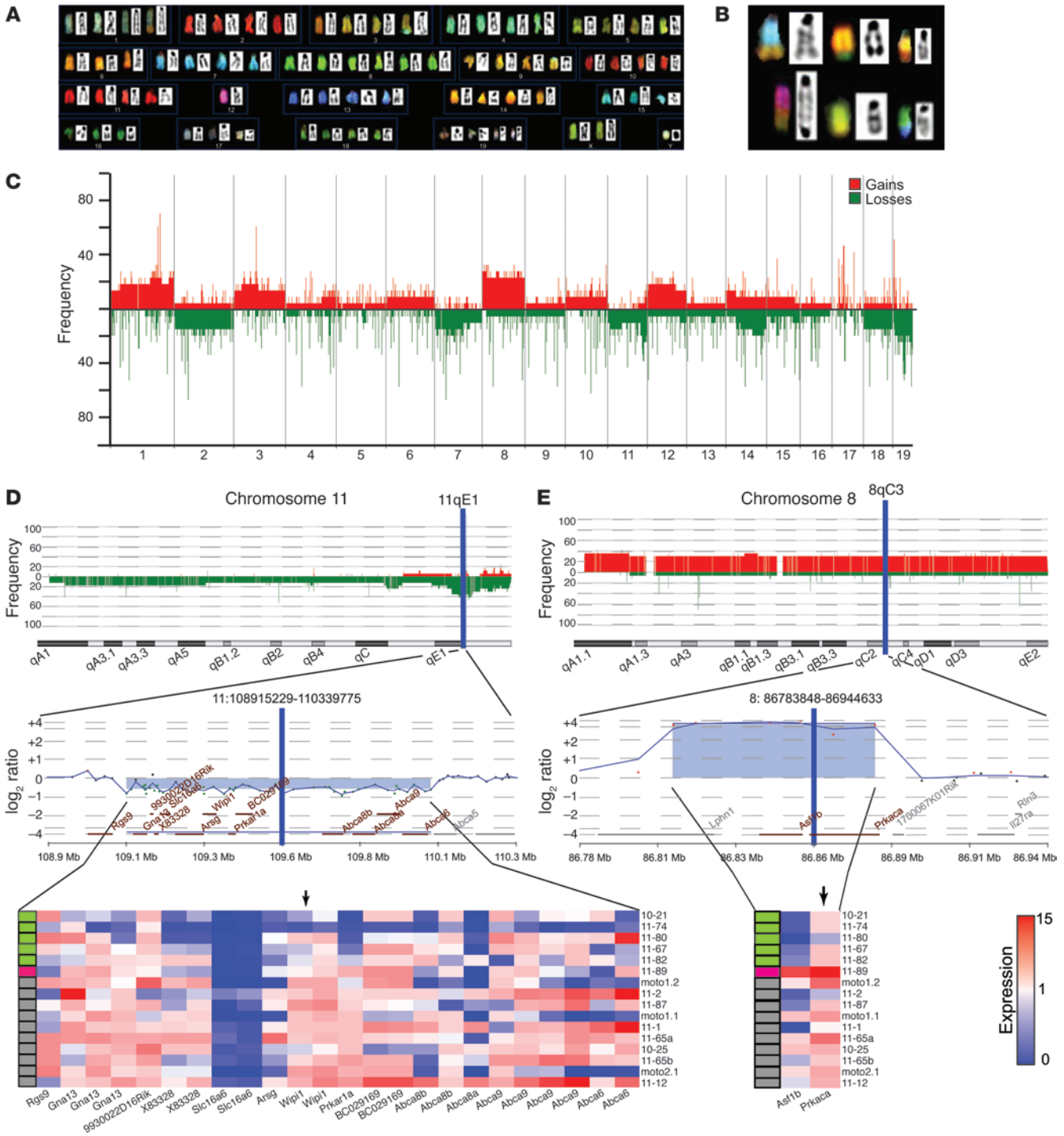

Figure 3

MOTO tumors exhibit genomic instability and PKA subunit gene CNAs. (**A**) Representative metaphase from SKY analysis of a MOTO tumor, displaying near tetraploid karyotype. (**B**) Nonrecurrent structural chromosomal aberrations in a primary tumor (top row), cell line (moto1.1; bottom row, left), and lung metastasis (bottom row, middle and right). (**C**) High-resolution aCGH on 14 MOTO OSA tumors and 3 moto cell lines. Data plotted are the aberration frequency across the autosomal chromosomes; chromosomes X and Y are not shown. Red bars indicate copy number gains; green bars indicate copy number losses. Each numbered segment along the *x* axis defines a block of data, corresponding to the indicated autosomal chromosome. (**D**) Integrative DNA-RNA analysis of sample-matched OSA shows concurrent deletion/underexpression of *Prkar1a* at 11qE1 or (**E**) focal amplification/overexpression of *Prkaca* at 8qC3. Top and middle panels contain frequency plots for CNAs and representative aCGH probe level aberration plots for the enlarged regions in question. Bottom panels show heat maps for the expression of genes within each region normalized to WT bone (black arrows indicate *Prkar1a* and *Prkaca*). Colored rectangles in **D** and **E** indicate the type of PKA CNA for each sample (green indicates *Prkar1a* deletion; red indicates *Prkaca* amplification; and gray indicates no PKA subunit gene CNA).

was mapped to chromosome 14qE2-4 (Supplemental Figure 6). This promoter drives Cre expression in osteoblasts (40), resulting in deletion of the floxed 2nd exon of *Prkar1a* (ΔOB). Exon 2 contains the initiator ATG codon and is thus required for translation. We confirmed exon 2 deletion using PCR and found it to be bone specific (Figure 5, A and B). Strikingly, none of the MOTO mice heterozygous for *Prkar1a* (n = 14; *Prkar1a*$^{\Delta OB/+}$/MOTO$^+$ mice) survived past 5 weeks of age due to advanced OSA (Figure 5C), often in spine, which resulted in impaired mobility and paralysis. These mice exhibited multi-ostotic tumors in long and flat bones, including the skull, vertebrae, ribs, and tibia (Figure 5D, middle and bottom), but did not develop metastases at this early age. Littermates from control cohorts (Colα(I)Cre$^+$/MOTO$^+$ and *Prkar1a*$^{\Delta OB/+}$ mice) showed no gross skeletal lesions at this age (Figure 5, E and F). Furthermore, a temporal analysis of early lesion formation undertaken on MOTO mice using micro-CT revealed only minor bone aberrations at 6 weeks, marginal increases in trabecular bone mass and microscopic preneoplastic lesions at 12 weeks, and osteolytic tumors by 18 weeks of age (Figure 5, G–I). Overall, the failure of *Prkar1a*$^{\Delta OB/+}$/MOTO$^+$ mice to survive past 5 weeks of age strongly contrasted with the control cohorts, which did not succumb to OSA until approximately 22 weeks of age (Figure 5C; $P < 0.0001$). Additionally, aCGH analysis of *Prkar1a*$^{\Delta OB/+}$/MOTO$^+$ tumors (n = 5) failed to indicate further deletions at 11qE1, suggesting *Prkar1a* loss of heterozygosity did not occur during tumorigenesis (data not shown).

Histological analyses of lesions were conducted across experimental and control cohorts. OSAs in 5-week-old *Prkar1a*$^{\Delta OB/+}$/MOTO$^+$ mice were similar to those observed in MOTO mice that were more than 20 weeks old (Figure 6A and Supplemental Figure 2, I–P) and expressed alkaline phosphatase (Supplemental Figure 2Q). Judged using qPCR, TAg expression was comparable among all MOTO$^+$ genotypes (Figure 6B). We next determined whether targeted *Prkar1a* heterozygosity drives RANKL transcription during tumorigenesis. RANKL was elevated in 3- to 4-week-old bones and overexpressed in tumors of *Prkar1a*$^{\Delta OB/+}$/MOTO$^+$ mice compared with those of MOTO$^+$ and WT controls (Figure 6C). Cell lines derived from *Prkar1a*$^{\Delta OB/+}$/MOTO$^+$ tumors also overexpressed RANKL at a level on par with that of moto2.1 cells (Figure 6C). Furthermore, we found that RANKL was highly elevated in the serum of *Prkar1a*$^{\Delta OB/+}$/MOTO$^+$ mice (Figure 6D), as has been reported in a study of human OSA patients (41). Using Western blotting, we observed high levels of phospho-CREB in 7 individual *Prkar1a*$^{\Delta OB/+}$/MOTO$^+$ tumor cell lines (Figure 6E); moreover, this was seen in *Prkar1a*$^{\Delta OB/+}$/MOTO$^+$ tumors and occasionally in tumors from control MOTO mice, consistent with our original hypothesis of a PKA$^+$ OSA subset in this model (Figure 6F). Phospho-CREB could be detected by immunostaining in *Prkar1a*$^{\Delta OB/+}$ bones, and was abundant in *Prkar1a*$^{\Delta OB/+}$/MOTO$^+$ tumors, but was absent in 3-week-old WT and MOTO bones (Figure 6G). To directly test the effects of *Prkar1a* heterozygosity on PKA activity, we used adenovirus to express Cre/GFP or GFP alone in primary osteoblasts cultured from *Prkar1a*$^{fl/+}$ bones (Figure 6H). We found the loss of a single *Prkar1a* allele to be capable of inducing an increase in PKA activity, indicating haploinsufficiency in the control of PKA signaling in osteoblasts (Figure 6I). Together, these experiments establish *Prkar1a* as a tumor suppressor in OSA. Deregulation of PKA signalling due to the loss of a single allele of this critical regulatory subunit causes RANKL overexpression.

Osteoblast-specific loss of Prkar1a initiates bone tumors independent of TAg. *Prkar1a*$^{\Delta OB/+}$ mice lacking the MOTO transgene were next followed over a longer period. We observed tumors at locations across the skeleton in all mice examined, showing *Prkar1a* heterozygosity to be capable of bone tumor initiation independent of T antigen (Figure 7, A and B). Previously Pavel et al. reported osteoblastic neoplasia in the tails of mice bearing full-body *Prkar1a* heterozygosity (42). We found homozygous osteoblastic deletion of this gene in *Prkar1a*$^{\Delta OB/\Delta OB}$ mice to be postnatally lethal within 24 hours (our unpublished observations). In *Prkar1a*$^{\Delta OB/+}$ mice, tumors could be detected by 10 weeks of age, with most mice having a tumor of at least of 2-mm diameter by 40 weeks (Figure 7, B and C). These lesions grew slowly, with 25% of mice bearing 8-mm tumors by 50 weeks of age. Without exception, *Prkar1a*$^{\Delta OB/+}$ mice developed tumors located in bone and did not develop metastases. The lesions were not typical OSAs, in that they did not appear to be composed of malignant osteoblasts depositing osteoid. Rather, the lesions consisted of an enlarged marrow space filled with abundant myxoid matrix, containing small fibroblast-like cells surrounded by trabecular-like bone, lined by plump, reactive, but otherwise normal osteoblasts in addition to regions with abundant osteoclasts (Figure 7D, left). Interestingly, myxomatous matrix was also present in some regions of the marrow in *Prkar1a*$^{\Delta OB/+}$/MOTO mice. In *Prkar1a*$^{\Delta OB/+}$ mice, the bone within and around the lesions was normal in appearance and contained osteocytes but seemed to be undergoing extensive remodeling (Figure 7D, right), perhaps in response to the expanding myxoid matrix filling the marrow cavity. Consistent with our findings of elevated phospho-CREB and RANKL overexpression in MOTO PKA$^+$ and *Prkar1a*$^{\Delta OB/+}$/MOTO tumors, *Prkar1a*$^{\Delta OB/+}$ tumors also had high phospho-CREB (Figure 6, F and G) and RANKL expression (Figure 7E). Furthermore, TRAP immunohistochemistry showed the presence of abundant osteoclasts in tumors from all genotypes (Figure 7F). Measurement of TRAP in the serum by ELISA indicated a significant increase in osteoclasts in MOTO mice compared with their WT controls, both at 12 and 18 weeks of age (Figure 7G). This was also noted in young 5-week-old tumor-bearing *Prkar1a*$^{\Delta OB/+}$/MOTO mice as well as aged *Prkar1a*$^{\Delta OB/+}$ 30-week-old mice.

Loss of PKA R1α instructs spontaneous OSA subclass development. We tested the directive capacity of *Prkar1a* alterations, during spontaneous subclass development in our mouse model, specifically whether *Prkar1a* loss in osteoblasts generates tumors with the transcriptional characteristics of the PKA$^+$ subclass. An expression signature was obtained by comparing MOTO PKA$^+$ to PKA$^-$ OSAs (508 genes, 5% FDR; Supplemental Table 4) and used in an unsupervised analysis of *Prkar1a*$^{\Delta OB/+}$/MOTO$^+$ tumors (n = 4) profiled by microarray. K-means clustering predicted these tumors to be PKA$^+$. Similarly, principal component analysis separated *Prkar1a*$^{\Delta OB/+}$/MOTO$^+$ OSAs from PKA$^-$ along the first principle component axis (72.7% variance explained) and grouped them with PKA$^+$ tumors (Figure 8A). Hierarchical clustering mirrored these results and showed *Prkar1a*$^{\Delta OB/+}$/MOTO$^+$ tumors to display a similar reciprocal pattern of gene expression to that of PKA$^+$ samples (Figure 8B). Thus, the loss of *Prkar1a* induces a broad transcriptional shift during tumorigenesis, resulting in the formation of a molecularly defined OSA subclass.

We next investigated whether a similar human OSA subset could be exposed by examining the features of tumors with low levels of *PRKAR1A* expression, using a recently published microarray data set (n = 34 pretreatment OSAs reported in ref. 43) and

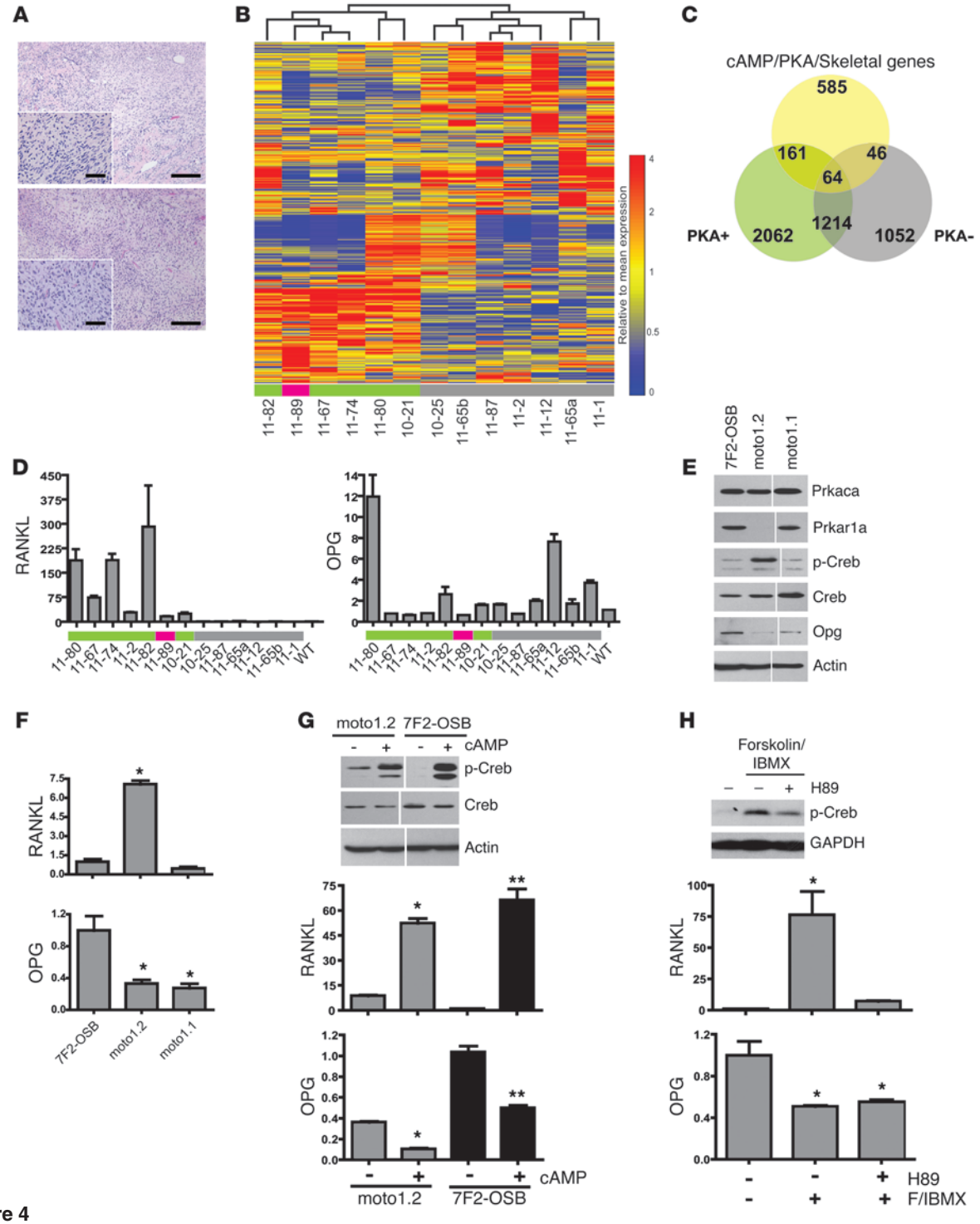

Figure 4

A molecularly defined mouse OSA subclass exhibiting RANKL overexpression. (**A**) PKA$^+$ and PKA$^-$ mouse OSAs show equivalent histological characteristics. Shown are H&E-stained end stage tumors from MOTO mice of more than 20 weeks of age in the PKA$^-$ (top) and PKA$^+$ (bottom) groups. Scale bars: 50 μm. (**B**) Unsupervised analysis using the cAMP/PKA/skeletal gene set for 13 MOTO OSA tumors highlights distinct subclass representing PKA CNAs (green indicates *Prkar1a* deletion; red indicates *Prkaca* amplification; and gray indicates no PKA CNA). (**C**) Three-way overlap of overexpressed or underexpressed genes in the PKA$^+$, PKA$^-$ MOTO OSA, and the cAMP/PKA/skeletal gene set. (**D**) qPCR of RANKL and OPG RNA in WT bone and 13 MOTO tumors (colored rectangles are same as in **B**). (**E**) Western blots and (**F**) qPCR of the indicated molecules in the 7F2-OSB and moto cell lines. (**G**) Western blots of total and phospho-CREB protein in cells treated with (+) or without (–) 1.5 mM cAMP for 30 minutes, and qPCR shows the effect of 8-hour cAMP treatment on RANKL and OPG. (**H**) Effect of 30 minutes 25 μM Forskolin/40 μM IBMX with or without 30 μM H89 treatment on phospho-CREB levels and on the expression of RANKL and OPG. Endogenous actin or GAPDH serve as protein loading controls. All analyses were performed in triplicate on 3 separate occasions; the hairline divider indicates samples run on the same blot. *$P < 0.05$ and **$P < 0.01$ indicate significance relative to 7F2-OSB or to untreated control. Data are represented as mean ± SEM.

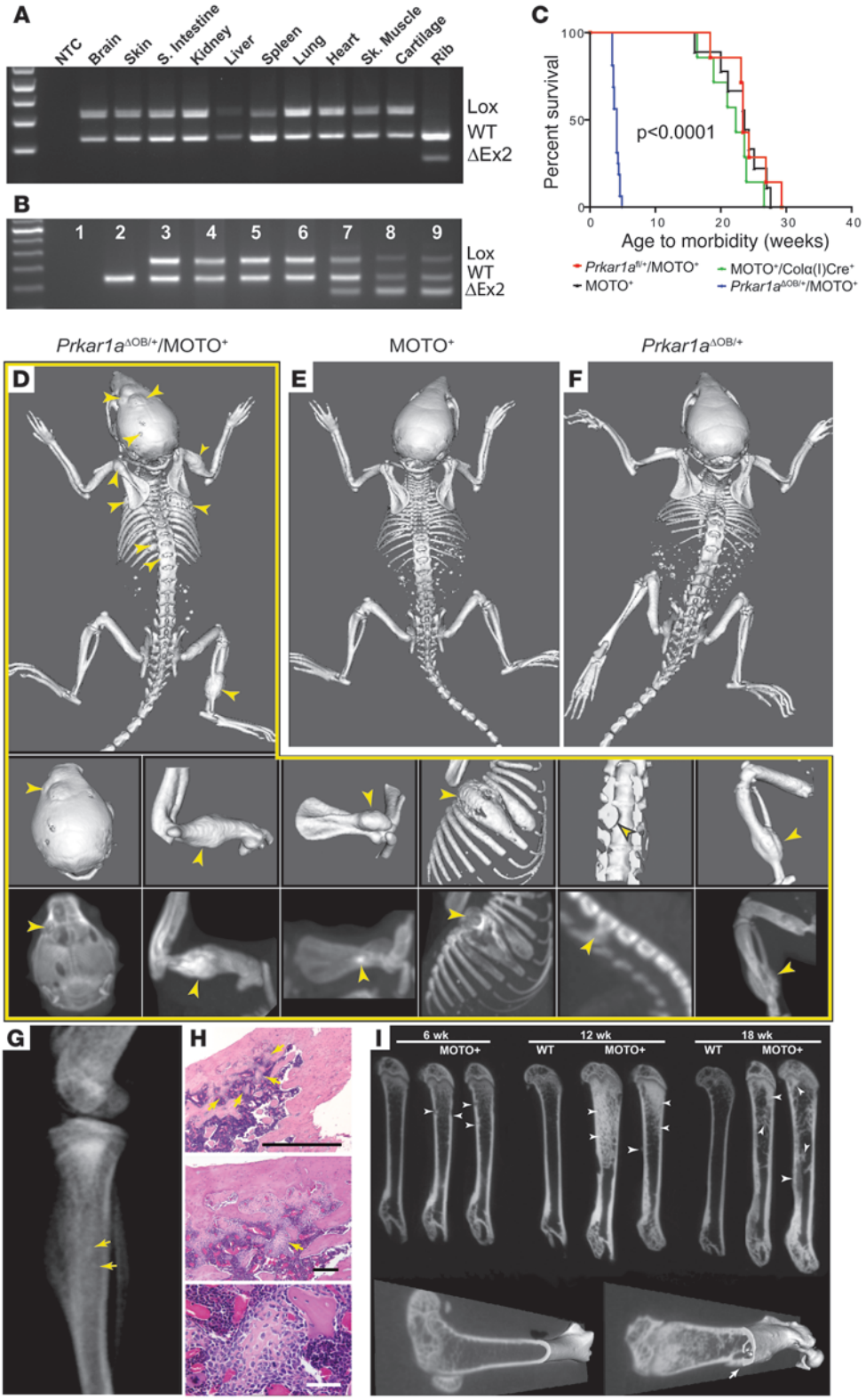

Figure 5

Prkar1a heterozygosity accelerates OSA development. (**A**) Genomic PCR showing bone-specific Cre-mediated *Prkar1a* exon 2 deletion (ΔEx2) in tissues from a *Prkar1a*$^{\Delta OB/+}$/MOTO^{-} mouse and (**B**) in normal and tumor-bearing mouse tissues (sample 1, no template control [NTC]; 2, WT femur; 3, *Prkar1a*$^{\Delta OB/+}$/MOTO^{+} lung; 4, *Prkar1a*$^{\Delta OB/+}$/MOTO^{+} spleen; 5, *Prkar1a*$^{flox/+}$/*Col*α(I)Cre^{-} femur; 6, *Prkar1a*$^{flox/+}$/*Col*α(I)Cre^{-}/MOTO^{+} femur; 7–9, *Prkar1a*$^{\Delta OB/+}$/MOTO^{+} femur, skull tumor, and tibial tumor, respectively. S. intestine, small intestine; Sk. muscle, skeletal muscle. (**C**) Kaplan-Meier plot of age to morbidity for the indicated control and experimental cohorts. Full-body skeleton CT scans of 3- to 4-week-old (**D**) *Prkar1a*$^{\Delta OB/+}$/MOTO^{+}, (**E**) MOTO^{+}, and (**F**) *Prkar1a*$^{\Delta OB/+}$ mice. Tumor-bearing bones of *Prkar1a*$^{\Delta OB/+}$/MOTO^{+} mouse in **D** are shown at higher magnification in middle panels (skull, humerus, scapula, rib, spine, and femur/tibia), with matching maximum intensity projections shown in bottom panels. (**G**) Radiograph of tibia of a 12-week-old mouse with abnormal growths (punctate densities), with corresponding H&E-stained sections (**H**) showing benign osteomas. Scale bars: 1 mm (top); 150 μm (middle); 50 μm (bottom). (**I**) Micro-CT images of femurs in 6- to 18-week-old mice. Images through the sagittal plane (top) reveal anomalous thickening of trabeculae and/or cortex (arrowheads) at 6 weeks of age and progressively more radiodense regions (arrowheads) at 12 and 18 weeks. 3D reconstructions of 18-week-old WT and MOTO (right) femurs show a parosteal tumor (arrow) with destroyed underlying cortex. Arrows indicate lesions throughout.

additional tumors (n = 20) generated by our group. Chemotherapeutic response data was available for 44 patients (responders, ≤2% tumor remaining after chemotherapy; nonresponders, >2% tumor remaining after chemotherapy). Samples were annotated according to expression quartiles for *PRKAR1A* and *PRKACA* (Figure 9A), and the response to therapy was compared among patients with *PRKAR1A*-low OSA (Q1; n = 14) and others (Q2–4; n = 40). Notably, the likelihood of responding to chemotherapy was significantly great-

er in patients with *PRKAR1A*-low tumors, using 2-tailed Fisher's exact test ($P = 0.0305$; odds ratio, 6.1; 95% CI, 1.340–28.07); similarly, median dichotomization of patients according to *PRKAR1A* expression showed the likelihood of responding to chemotherapy to be 4.9-times higher for those with *PRKARIA*-low OSA ($P = 0.0305$; 95% CI, 1.324–18.21). Conversely, tumors that responded to chemotherapy showed significantly lower *PRKAR1A* expression ($P = 0.0106$; Figure 9B). Analysis of overall patient survival and *PRKAR1A* expression did not indicate a correlation.

To examine whether human *PRKAR1A*-low tumors are transcriptionally distinct from other OSAs, an unsupervised analysis was performed using orthologs for the cAMP/PKA/skeletal gene set. This distinguished a cluster dominated by *PRKAR1A*-low tumors (Figure 9C) but not *PRKACA*-low or -high tumors. Additionally, annotation of the samples with expression quartiles for the other 5 PKA subunit genes did not reveal further associations (Supplemental Figure 7). We also asked whether human *PRKAR1A*-low and mouse PKA$^+$ tumors possess similar indicators of PKA pathway alteration. Expression signatures for human *PRKAR1A*-low and mouse PKA$^+$ OSA (including *Prkar1a*$^{\Delta OB/+}$/MOTO$^+$ mice) were generated, yielding upregulated/downregulated genes (humans, 3,226 upregulated/2,115 downregulated genes; mice, 563 upregulated/668 downregulated genes; 5% FDR), and analyzed for enrichment in gene ontology (GO) terms within the cAMP/PKA/skeletal gene set. Signatures in both species were enriched for genes functioning in "positive regulation and activation of adenylate cyclases" and "G protein signaling coupled to cAMP" (Supplemental Table 5; $P < 0.05$) but not negative regulation of these processes. The upregulated genes for the mouse and human subsets also displayed parallels for a broader set of enriched functional gene sets (Supplemental Table 6), with downregulated genes showing more functional diversity across species (Supplemental Table 7). In this human OSA data set, RANKL was overexpressed in *PRKAR1A*-low tumors, but this overexpression was not limited to samples in this quartile, unlike in MOTO mice in which RANKL overexpression was largely restricted to the PKA$^+$ subtype. It is possible that other mechanisms are involved in inducing RANKL overexpression in human OSA, outside of the *PRKAR1A*-low subset. Wnt and Hh (hedgehog) signaling control RANKL expression, the latter through PTHrP (44), offering multiple avenues for RANKL induction in addition to PKA deregulation; Wnt inhibitory factor 1 was recently found to be epigenetically silenced in human OSA, and its loss accelerates development of radiation-induced OSA in mice (45). These analyses raise the possibility that low levels of *PRKAR1A* expression associate with a molecularly distinct subset of human OSA. Additionally, the clinical behavior of these tumors is suggestive of fundamental biological differences from other OSAs.

Discussion

Here we model human OSA in a genetically engineered mouse and use an iterative approach to identify tumor subtypes and pathogenetically relevant genes in OSA. A subclass of OSA arises in the MOTO model that exhibits recurrent deletions at 11qE1, targeting *Prkar1a*, PKA signaling deregulation, and RANKL overexpression. Heterozygous loss of *Prkar1a* directs subclass formation and radically accelerates OSA development, exposing it to be a tumor suppressor in this cancer. Guided by these findings, we uncovered evidence for a *PRKAR1A*-low molecular subclass of human OSA, with distinct clinical behavior.

PKA signaling in osteoblasts is the canonical pathway for PTH regulation of bone turnover, and of the 4 PKA regulatory subunits, only *PRKAR1A* is essential for development and cAMP regulation (46). PKA regulatory subunits are differentially expressed across tissues, with RIα and RIIα being ubiquitous and R1β and RIIβ showing a more restricted pattern (46). As a component of type I PKA, RIα is linked to the control of cell proliferation and neoplastic transformation (47). In emerging data related to catalytic PKA subunits, combined deletion of Cα with RIα was recently shown to result in a shift to type II PKA signalling (48). In our study we found *Prkaca* amplification in one OSA, and the role of this catalytic subunit requires further investigation. In spite of supporting evidence from human genetics, a role for *PRKAR1A* in bone tumorigenesis is only beginning to be recognized. Germline *PRKAR1A* mutations cause the Carney Complex (49), an autosomal dominant multiple neoplasia syndrome that occasionally features osteochondromyxomas (50); consistently, aged *Prkar1a*$^{+/-}$ mice develop benign osteoblastic lesions of the tail vertebrae (42). In *Prkar1a*$^{\Delta OB/+}$ mice, we observed an expanded skeletal tumor distribution to that reported for germline *Prkar1a*$^{+/-}$ and compound *Prkar1a*$^{+/-}$*Prkaca*$^{+/-}$ mice (42, 48); indeed we found tumors to arise across the skeleton, including both long and flat bones, and tumors were not restricted to the tail as is seen in *Prkar1a*$^{+/-}$ mice. During characterization of *Prkar1a*$^{\Delta OB/+}$ mice, we observed a lack of Cre-mediated *Prkar1a* recombination in cartilage, indicating that chondrocytes are not affected; notably, the myxomatous tumors that developed in *Prkar1a*$^{\Delta OB/+}$ mice did not show a cartilaginous component, as has been recently reported in the osteochondromyxomas that develop in *Prkar1a*$^{+/-}$*Prkaca*$^{+/-}$ mice. Consistent with the dramatic acceleration of OSA development we observed in *Prkar1a*$^{\Delta OB/+}$/MOTO mice, Almeida et al. recently described generally increased tumorigenesis in *Trp53*$^{+/-}$ and *Rb1*$^{+/-}$ mice when combined with *Prkar1a* heterozygosity (51); here, *Trp53*$^{+/-}$*Prkar1a*$^{+/-}$ mice developed significantly more OSAs. In human OSA, the observed correlation of low levels of *PRKAR1A* expression and good response to chemotherapy may suggest these tumors to be highly proliferative. There is some evidence suggesting that highly proliferative OSA tumors may be better targeted by the chemotherapeutics used in this cancer (52). Though we observed tumors in MOTO/*Prkar1a*$^{\Delta OB/+}$ mice to be fast growing, this may be reflective of a high proliferation index, decreased cell death, or increased bone turnover, and therefore additional work will be required to explore this relationship. Furthermore, an important next question is whether correlations are found between p53/Rb status and PKA pathway activation via possible *PRKAR1A* alterations in human OSA. Interestingly, postzygotic *GNAS1* mutations in McCune-Albright syndrome patients lead to uncontrolled cAMP signaling, causing polyostotic fibrous dysplasias (53), and the development of OSAs in these patients have been noted (54, 55). Our demonstration that loss of *Prkar1a* drives malignant OSA tumorigenesis unifies these observations in skeletal biology and disease.

Given the many targets of PKA signaling, we looked to bone biology in our search for critical oncogenic effectors of PKA deregulation during OSA development. By restricting our analysis to a tissue-associated gene set, RANKL emerged as a promising candidate. Other regulators of RANKL expression in osteoblasts include Wnt and Hh, the latter by controlling PTH-related peptide expression (44). In bone, RANKL signals through RANK, a receptor expressed by osteoclasts. The RANKL/OPG/RANK triad constitutes a system that functionally couples osteoblasts and osteoclasts, the 2 major bone cell types (56). RANK

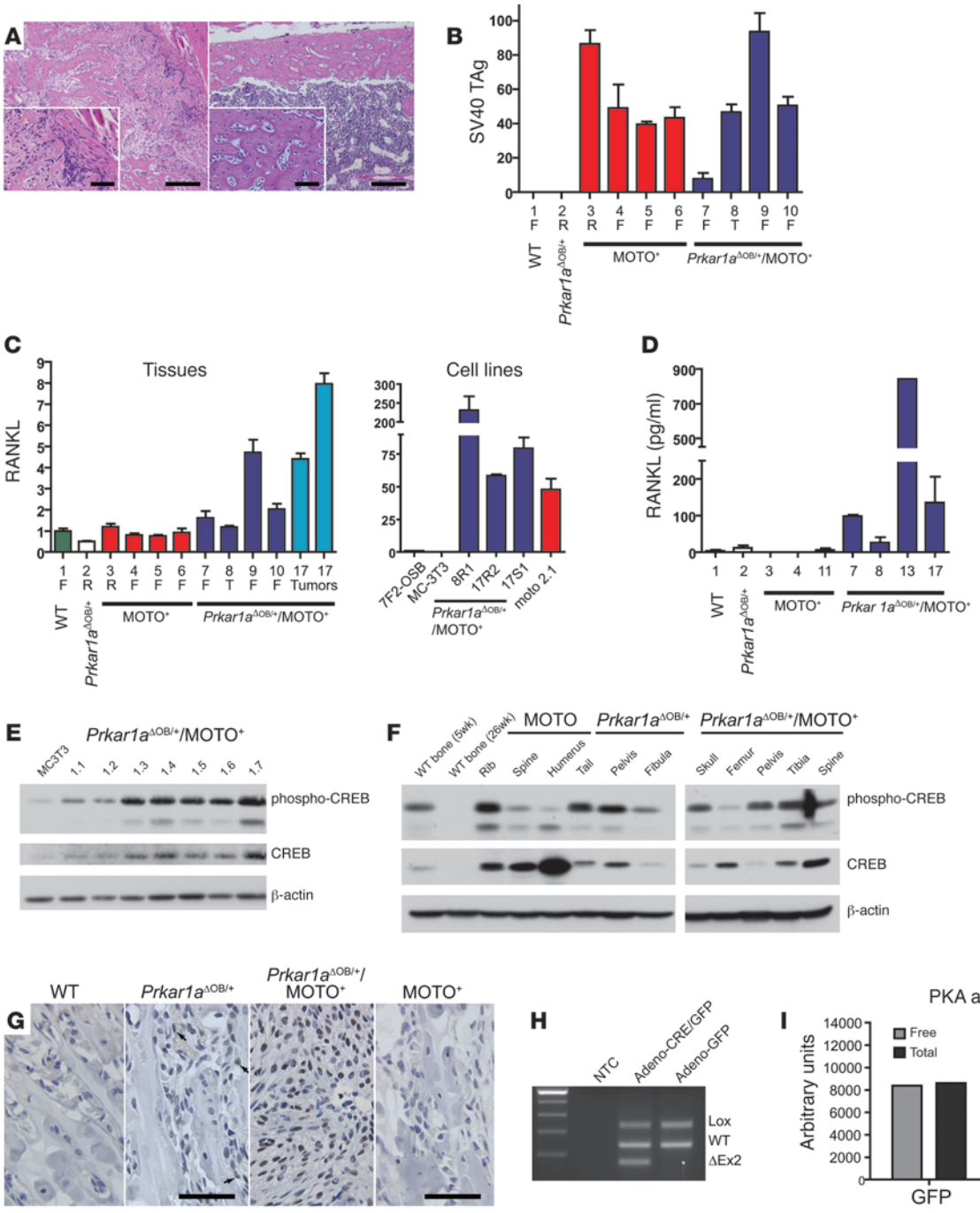

Figure 6

Deregulated PKA signaling drives RANKL overexpression during OSA development. (**A**) H&E staining of (left) OSA in *Prkar1a*$^{\Delta OB/+}$/MOTO^{+} tibia and (right) tumor-free femur from age-matched MOTO^{+} mouse. (**B**) qPCR of SV40 TAg in samples from 3- to 4-week-old mice. (**C**) qPCR of RANKL RNA in bone samples of 3- to 4-week-old MOTO^{+} and *Prkar1a*$^{\Delta OB/+}$/MOTO^{+} mice and tumor cell lines from *Prkar1a*$^{\Delta OB/+}$/MOTO^{+} mice (rib, 8R1 and 17R2; skull, 17S1), moto2.1, and control MC-3T3 and 7F2-OSB cells. (**D**) Serum RANKL analysis by ELISA in 3- to 4-week-old mice of indicated genotypes. F, femur; R, rib; T, tibia; Tumors, rib and tibia. (**B**–**D**) Numbers identify the same individual mice across panels. (**E**) Western blots showing total and phospho-CREB protein in cell lines derived from *Prkar1a*$^{\Delta OB/+}$/MOTO^{+} bone tumors and MC3T3 cells and (**F**) tumors from the indicated genotypes. Endogenous actin was used as protein loading control. (**G**) Phospho-CREB immunostaining of femurs of control mice of the indicated genotypes (WT, *Prkar1a*$^{\Delta OB/+}$, and MOTO^{+} mice), and a skull tumor from a *Prkar1a*$^{\Delta OB/+}$/MOTO^{+} mouse. Arrows highlight cells with low phospho-CREB staining; strong staining appears in the tumor. (**H**) Genomic PCR for CRE-mediated floxed exon 2 deletion in primary osteoblast cultures from *Prkar1a*$^{fl/+}$ mouse bones treated with recombinant adenoviral CRE-GFP or control GFP expression construct. (**I**) PKA activity from Adeno-Cre/GFP– or GFP-treated primary osteoblasts cultured from *Prkar1a*$^{fl/+}$ bones was measured either in the absence of exogenous cAMP (free PKA activity) or in the presence of 25 μM cAMP (total PKA). Scale bars: 150 μm (**A**); 50 μm (**A**, insets, and **G**). Data are represented as mean ± SEM.

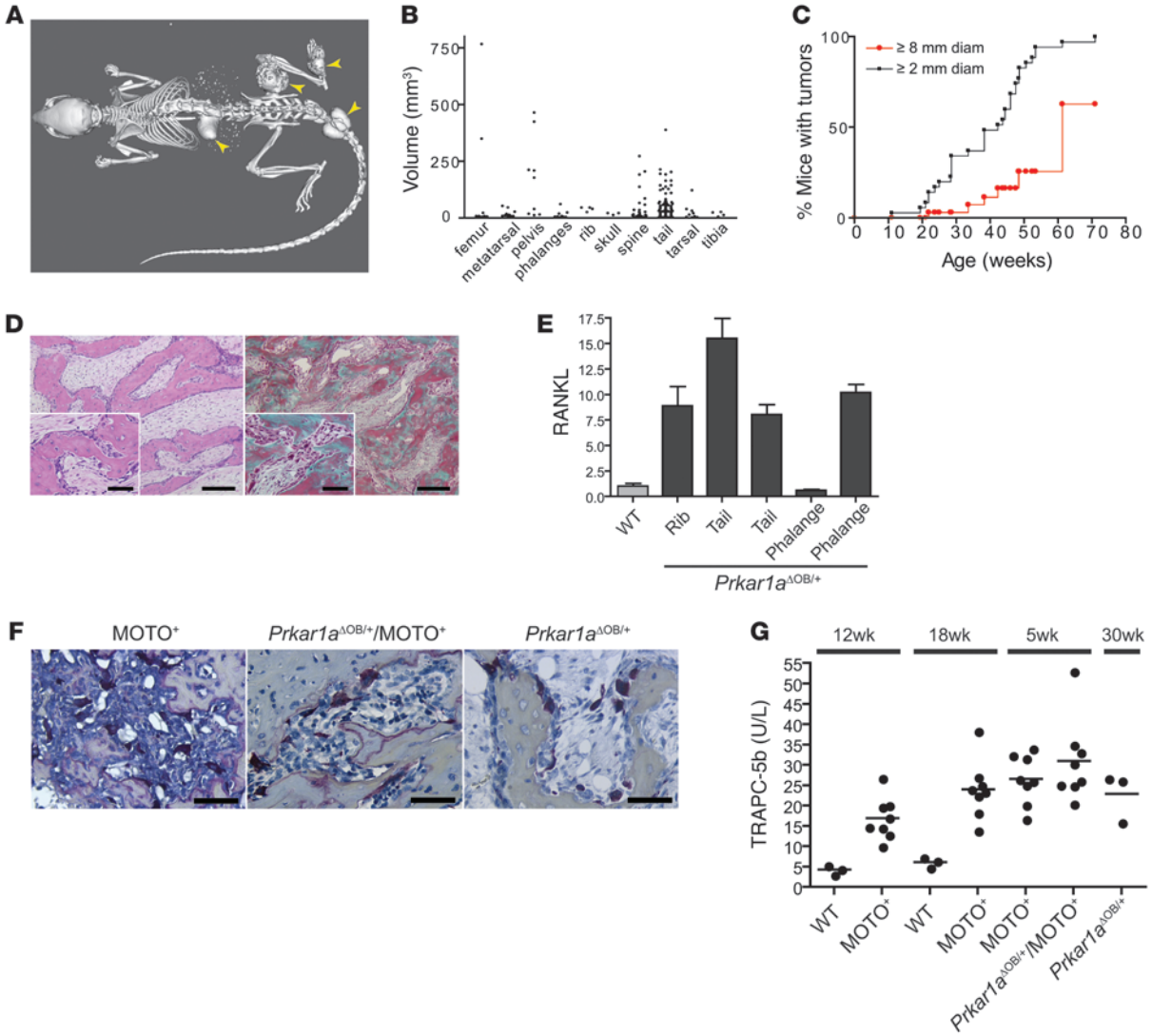

Figure 7

Bone tumorigenesis resulting from conditional heterozygous osteoblastic *Prkar1a* loss in mice. (**A**) Full-body CT scan of a 33.6-week-old *Prkar1a*$^{\Delta OB/+}$ mouse with bone tumors in the femur, spine, tail, and metatarsals (arrowheads). (**B**) The frequency and size of bone tumors occurring at the indicated skeletal sites are plotted for 282 lesions measured from x-ray radiographic images from a group of 25 *Prkar1a*$^{\Delta OB/+}$ mice at 11–71 weeks of age. The majority are lesions in the vertebrae of the tail and spine, with the largest occurring in the femurs and pelvis. Each dot represents an individual bone tumor. (**C**) A Kaplan-Meier plot represents the percentage of mice whose largest tumor was greater than 2 mm in diameter (black line) or 8 mm in diameter (red line). (**D**) H&E (left) and Masson's trichrome (right) staining of a paraffin sections of a femur tumor from a 49.1-week-old *Prkar1a*$^{\Delta OB/+}$ mouse. (**E**) qPCR of RANKL RNA in bone tumor samples from indicated skeletal sites from 58.4- and 74.6-week-old *Prkar1a*$^{\Delta OB/+}$ mice and a WT control. Data are represented as mean ± SEM. (**F**) TRAP histochemical stains of a 22.4-week-old MOTO$^+$ rib tumor (left), a 3.7-week-old *Prkar1a*$^{\Delta OB/+}$/MOTO$^+$ tibia tumor (middle), and 49.1-week-old *Pkrar1a*$^{\Delta OB/+}$ femur tumor (right) show abundant osteoclasts. (**G**) ELISA for osteoclast-derived TRAPC-5b in the serum of mice of indicated genotype and age. Each dot represents an individual mouse, and horizontal lines in each column represent the median. Scale bars: 150 μm (**D**); 50 μm (**D**, insets, and **F**).

expression in the bone is normally restricted to preosteoclasts and osteoclasts, which depend on osteoblast-derived RANKL for their differentiation and activation (56). Indeed, RANKL is an essential regulator of osteoclast differentiation, and *Tnfsf11*$^{-/-}$ mice are severely osteopetrotic, due to a lack of osteoclasts (57). RANKL is highly expressed in OSA (33), and functional RANK expression has been reported in human primary OSA and cell lines (58). In the current study, RANKL overexpression was found to be driven by deregulated PKA signaling in vitro and in vivo, both in OSAs and benign myxomatous bone tumors. The intermittent or continuous stimulation of osteoblasts with PTH through the PKA pathway differentially induces an anabolic or catabolic effect (59), and interestingly, OSA lesions are observed to be osteolytic and osteoid depositing (60). RANKL is emerging as a promising target in bone disease, and specific agents for this molecule are approaching the clinic (61). Our data support its investigation as a tractable target in OSA therapeutics downstream of deregulated osteoblastic cAMP/PKA signaling.

Major strides are being made to address human cancer diversity. Efforts are aimed at identifying molecular subclasses using

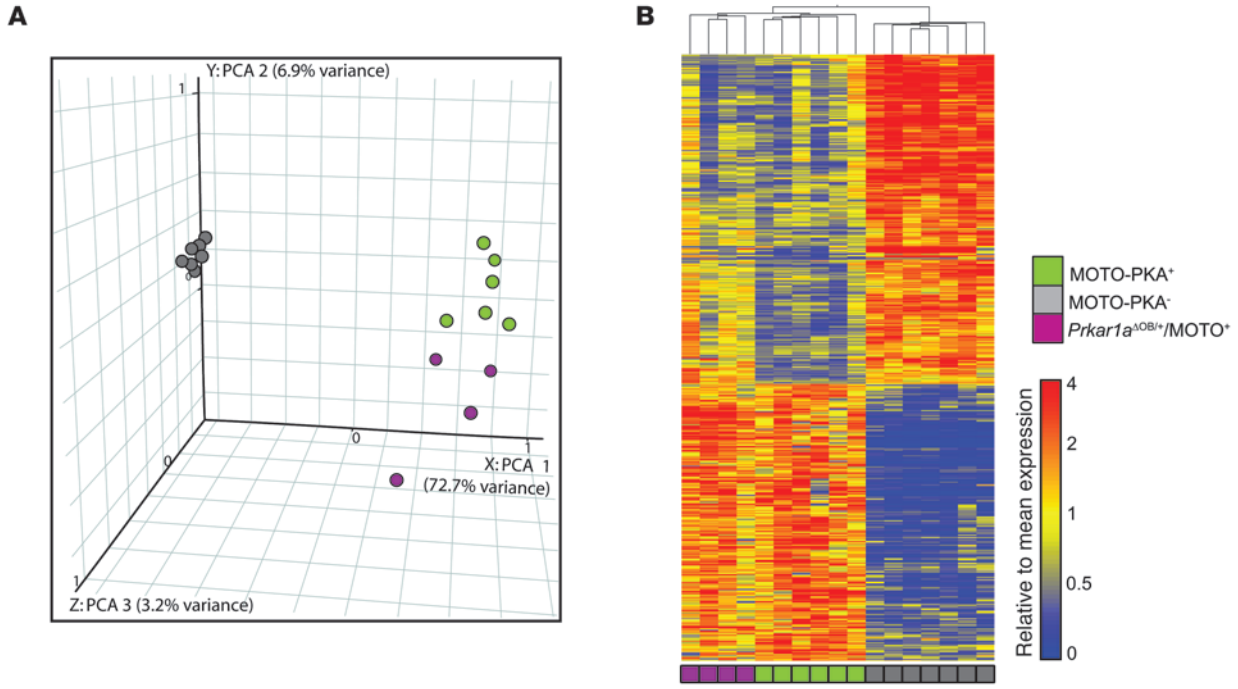

Figure 8
Prkar1a heterozygosity instructs a widespread transcriptional shift during spontaneous tumorigenesis. (**A**) Principle component analysis (PCA) and (**B**) hierarchical clustering of PKA$^+$, PKA$^-$, and *Prkar1a*$^{\Delta OB/+}$/MOTO$^+$ tumors, using a 508 gene-training signature. All *Prkar1a*$^{\Delta OB/+}$/MOTO$^+$ mice were 3.4–4.7 weeks of age.

genome-wide profiling (2, 3) as exemplified by the 5 breast cancer subtypes, matching mouse models to subclasses within human histopathological groups (9, 10), and the development of mouse models that are predictive of chemotherapeutic response in patients (1). On the other hand, the cancer heterogeneity inherent to mice is just beginning to be explored; this was examined in mammary tumor models, suggesting a claudin-low subtype in breast cancer (9) as well as in the Eμ-myc model of B cell lymphoma (62). We took advantage of heterogeneity among tumors in the MOTO model, as part of an iterative approach to expose concealed molecular phenotypes and their respective driver genes in OSA. We show that histologically similar but molecularly distinct tumor subclasses can be identified in mice on the basis of their association with recurrent mutations such as gene deletion. Pinpointing *Prkar1a* allowed us to evaluate it as a candidate driver gene based on its capacity to potentiate tumor formation as well as to cause a broad transcriptional shift during spontaneous tumorigenesis toward that of tumors with 11qE1 deletion. This demonstrates that tumor subclass formation in mice can be experimentally directed through early introduction of key alterations. Importantly, mouse subclasses can potentially inform the stratification of cognate human tumors, offering leads at the level of a single driver gene or its pathway. We propose that tumor subsets exist within many mouse models and may be sought for this purpose.

Methods

Construct. A 2.7-kb sequence consisting of SV40 T/t antigen and a polyadenylation signal (a gift of U. Rüther, Heinrich Heine University, Düsseldorf, Germany) was cloned downstream of the 1.3-kb murine osteocalcin promoter (OG2; a gift of G. Karsenty, College of Physicians and Surgeons, Columbia University, New York, USA) by introducing SalI and EcoRI sites at the 5′ and 3′ ends using PCR. The 4-kb KpnI-EcoRI fragment was microinjected into fertilized zygotes of FVB mice. PCR screening of offspring yielded 3 founders, which were used to generate the independent lines MOTO-1, MOTO-2, and MOTO-3. The PCR primers, OG2, 5′-GCAATCACCAACCACAGCATC-3′, OCN, 5′-GGAGAAGACACACAAGGTCAGGTAA-3′, and TAg, 5′-TTCCCCCAGGCACTCCTTTC-3′, were used for genotyping and generating a 575-bp band for a WT osteocalcin sequence and a 315-bp band for the transgene. MOTO mice are maintained in a pure FVB background.

Mouse lines and tissue. MOTO mice were monitored weekly for tumor development and sacrificed upon signs of distress due to tumor and/or metastatic burden, impaired motility arising from spine or skull tumors, or feeding complications due to mandible tumors. *Prkar1a*$^{flox/+}$ mice (39) and Colα1(I)Cre mice (40), both in FVB, were crossed with MOTO mice and studied as heterozygotes for *Prkar1a*. Survival statistics were calculated using the log-rank test. Mouse tissues were fixed in formalin or 4% paraformaldehyde and paraffin embedded for histology. Midline longitudinal 5-μm sections of long bones were H&E stained and analyzed for bone lesions. Antibodies for immunohistochemistry included alkaline phosphatase (R&D Systems), phospho(ser133)-CREB (Cell Signaling Technology), and SV40 TAg (BD Pharmingen).

MOTO mice and ColIα(I)Cre mice are in the FVB background. *Prkar1a*$^{lox/lox}$ mice obtained from L.S. Kirschner have been crossed into the FVB background. Mice were bred by setting up the following breeding pairs: *Prkar1a*$^{lox/+}$/MOTO$^+$/Colα(I)Cre$^-$ males were bred with *Prkar1a*$^{lox/+}$/MOTO$^-$/Colα(I)Cre$^+$ females; *Prkar1a*$^{lox/lox}$/MOTO$^-$/Colα(I)Cre$^-$ females were bred with *Prkar1a*$^{+/+}$/MOTO$^+$/Colα(I)Cre$^+$ males; and occasionally *Prkar1a*$^{lox/+}$/MOTO$^-$/Colα(I)Cre$^+$ females were

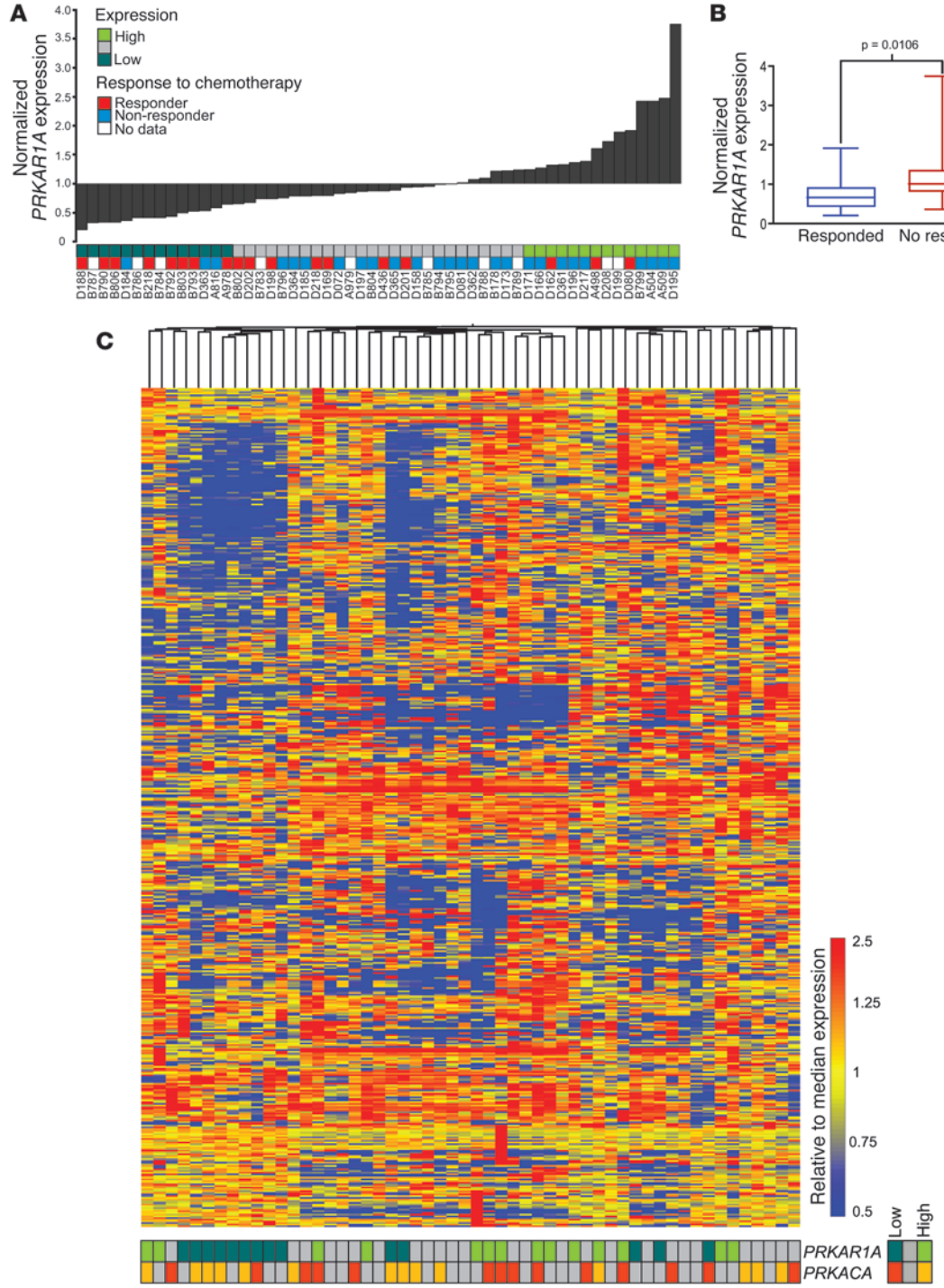

Figure 9

Evidence for a molecularly distinct *PRKAR1A*-low subset of human OSA. (**A**) *PRKAR1A* expression in 54 human OSAs, ranked low to high, with the lowest and highest 25% indicated. Response to chemotherapy is indicated by colored blocks. (**B**) The normalized expression level of *PRKAR1A* was compared between responders and nonresponders. Boxes depict IQR; lines within represent the median; whiskers denote maximum and minimum values. (**C**) Unsupervised analysis of human OSAs using hierarchical clustering. The cAMP/PKA/skeletal gene set (human orthologs) was used and samples were annotated according to low or high expression of *PRKAR1A* and *PRKACA* (below heat map).

bred with *Prkar1a*$^{lox/lox}$/MOTO^{+}/Colα(I)Cre^{-} males. The proper Mendelian ratios were obtained, with *Prkar1a*$^{lox/lox}$/Colα(I)Cre^{+} mice dying 1 day postnatally. The Cre-mediated *Prkar1a* exon 2 deletion PCR assay and *Prkar1a*$^{lox/lox}$ mouse genotyping were accomplished using the following primers: lox2B, GCAGGCGAGCTATTAGTTTA; lox1B, CAAGCTAGCTTGGCTGGACGTA; and lox4, CATCCATCTCCTATCCCCTTT. All animal experiments were approved by the Animal Care Committee of the Ontario Cancer Institute.

Cell culture. Primary mouse bone tumors were minced and plated in a low volume of media to generate OSA cell lines. These were maintained in DMEM media. Alkaline phosphatase immunostaining was performed using a Leukocyte Alkaline Phosphatase Kit (86C, Sigma-Aldrich). Mouse osteoblastic cells (7F2, MC-3T3) were obtained from ATCC (CRL-12557 and CRL-2593).

Imaging. For micro-CT imaging, formalin-fixed whole-mouse carcasses were placed in a GE Locus Ultra Micro-CT (GE Medical Systems) and subjected to a 16-second Anatomical Scan Protocol (total of 680 images) at 80 kV, 70 mA, using a 0.15-mm Cu Filter, to achieve approximately 150 micron resolution. For micro-CT imaging, fixed mouse femurs were immobilized in agarose. Specimens were scanned at 29 μm for 2 hours using a micro-CT scanner (GE eXplore Locus SP, GE Healthcare). Seven hundred and twenty views were acquired through 360-degree rotation with the x-ray source at 80 kVp and 80 μA. 3D micro-CT data were reconstructed at 58-μm resolution using the Feldkamp algorithm.

For second harmonic generation microscopy, images were generated for bone, lung, and liver from tumor-bearing mice using an 840-nm Chameleon Titanium-Sapphire mode-locked femtosecond laser and a Zeiss LSM 510 META NLO inverted laser scanning microscope. Bandpass filters of 430/75 (for SHG) and 525/50 (for tissue autofluorescence), in tandem with a long-pass 490-nm dichroic mirror, were used to capture the 2-color images of dual SHG and multiphoton tissue autofluorescence. Images were recorded, at identical laser intensities and photomultiplier tube gains, as a z stack of multiple individual x-y images at differing focal planes. These z stacks were subjected to average intensity projection and 2-channel intensity adjustment.

For x-ray imaging, live isoflurane-anesthetized mice were imaged using a MX-20 Radiography System (Faxitron X-ray Corp.) set at 24 kV, with a 4-second exposure time. Multiple images per mouse in 2 orientations were analyzed using Specimen DR version 3.2.2 software (Faxitron X-ray Corp.) to generate length (l), width (w), and height (h) measurements (in mm) for the diameter of each lesion, and tumor volume was estimated as the volume of an ellipsoid ($4/3\pi \times l \times w \times h$) where l, w, and h are radii. Thirty-five x-ray images were analyzed for 25 *Prkar1a*$^{\Delta OB/+}$ mice, with ages from 11 to 71 weeks of age; 282 lesions were measured. Kaplan-Meier curves were generated by assessing the age by which the largest tumor per mouse per time point imaged achieved a volume greater than 4.2 mm^3 or 268.1 mm^3, corresponding to tumors having diameters of 2 mm and 8 mm, respectively.

qPCR analysis, Western blotting, and ELISA. Total RNA was prepared from MOTO bones (flushed to remove bone marrow, flash frozen, and pulverized) or cell lines using TRIzol (Invitrogen). RNA purity was confirmed using a NanoDrop Spectrophotometer (Thermo Scientific). One μg of RNA was reversed-transcribed and subjected to qPCR (ΔΔCt), using an ABI PRISM 7900HT Sequence Detection System (Applied Biosystems) and TaqMan gene expression assay mix containing unlabeled PCR primers and FAM-labeled TaqMan MGB probes. Primers and probes are listed in Supplemental Methods (Supplemental Table 8). All raw data were analyzed using Sequence Detection System software version 2.1 (Applied Biosystems). The threshold cycle (C_T) values were used to calculate relative RNA expression levels. Values were normalized to endogenous 18S transcripts. Tissues and cell lines were processed for Western blotting using standard procedures. The antibodies used for Western blotting were as follows: mouse *Prkaca*, CREB, phospho(ser133)-CREB (Cell Signaling Technology Inc.), *Prkar1a* (Abcam Inc.), Opg (R&D Systems), and SV40 TAg (BD Pharmingen). Blots were reprobed with an HRP-conjugated β-actin antibody (Santa Cruz Biotechnology Inc.) to confirm protein loading. The SuperSignal West Pico Chemiluminescent Substrate system (Pierce Biotechnology Inc.) was used to visualize antibody bound antigen. For studies examining PKA signaling, moto1.2 and 7F2-OSB cells (1.2×10^5 cells/6-well plate) were cultured in complete media containing 1.5 mM 8-bromo-cAMP for 30 minutes. Moto1.2 cells were serum starved and treated with H89, Forskolin, and IBMX (Sigma-Aldrich). To determine association of SV40 TAg with p53 or Rb1 protein, agarose-conjugated monoclonal antibodies against p53 or Rb1 (Santa Cruz Biotechnology Inc.) were used. Immunoprecipitates were separated on PAGE gels, followed by immunoblotting for SV40 T antigen. IP confirmation was assessed by reprobing for Rb1 and p53, respectively. *ELISA* serum RANKL levels were measured using the commercial Quantikine precoated mouse RANKL ELISA kit (catalog MTR00, R&D Systems).

Copy number and transcriptional analysis. Genomic DNA from mouse tumors, cell lines, and pooled WT FVB tissue controls were extracted using phenol chloroform, treated with RNase A (Invitrogen) for 1 hour at 37°C, and profiled on Agilent 105K oligonucleotide CGH arrays at The Centre for Applied Genomics. The MOTO model is maintained in the pure FVB background, and aCGH control DNA was derived from littermate tails to minimize natural intrastrain genomic copy number variation. Mouse tumors, cell lines, and flushed normal bone total RNA was extracted using TRIzol (Invitrogen), analyzed for integrity using the Agilent Bioanalyzer (Agilent Technologies), and profiled on Agilent Mouse Whole-Genome 4x44K arrays at the University Health Network Microarray Centre.

Cytogenetics and transgene mapping. Fluorescence probe labelling and transgenic mapping by sequential G-banding to FISH were performed by The Centre for Applied Genomics. G-banding was performed using standard techniques. DNA isolated from BAC clones used as control probes was obtained from The Centre for Applied Genomics and directly labelled with SpectrumGreen-dUTP according to kit specifications. DNA isolated from OG2-SV40 Tag construct plasmid and Cre plasmids (a gift from Vuk Stambolic) were used as test probes and directly labelled with SpectrumOrange-dUTP according to kit specifications. FISH was carried out as previously described (63) on metaphase chromosomes using OG2-SV40 Tag and Puro-Cre test probes. For each experiment, the first FISH for each test probe was performed to identify the transgene insertion site by G-banding, and the second FISH for each test probe was cohybridized with a control probe to confirm the identity of the chromosome with transgene insertion. A minimum of 5 metaphases were examined per experiment using a MetaSystems Axioplan2 microscope and an Applied Spectral Imaging Olympus BX61 microscope, and images were captured using Isis and FISHView software, respectively.

Adenoviral infection and kinase activity assay. Mouse bone-derived cells were cultured from femurs and tibias of *Prkar1a*$^{\Delta OB/+}$ mice and treated with recombinant CRE/GFP or GFP adenoviral particles (Vector Biolabs) overnight at an MOI of 50. Forty-eight hours later, GFP expression was examined using fluorescence microscopy. PKA activity in osteoblast cultures was assessed using the PepTag nonradioactive cAMP-dependent protein kinase assay (Promega), following the manufacturer's instructions. Briefly, cells were washed twice with ice-cold PBS, and fresh protein lysates were harvested from stably GFP- or Cre-infected *Prkar1a*$^{loxp/loxp}$ osteoblasts, using a 25 mM Tris-HCl pH 7.4 extraction buffer containing EDTA (0.5 mM), EGTA (0.5 mM), β-mercaptoethanol (10 mM), leupeptin (1 μg/ml), aprotinin (1 μg/ml), and PMSF (0.5 mM). Lysates were homogenized on ice using a Dounce homogenizer and centrifuged for 5 minutes at 14,000 *g* at 4°C, and the supernatant was removed and quantified using a BCA protein assay kit (Pierce). Two micrograms of PepTag A1 Peptide were incubated with 2 μg protein lysate in a final volume of 25 μl for 30 minutes at room temperature alone, in the presence of 10 μg/ml PKI, 25 μM cAMP (8-(4-chlorophenylthio)adenosine 3′,5′-cyclic monophosphate sodium salt; Sigma-Aldrich), or PKI (Promega) and cAMP. The reactions were stopped by heating to 95°C for 10 minutes. The samples were separated on a 0.8% agarose gel at 100 V for 25 minutes. Phosphorylated peptide migrated toward the cathode (+), while non-

phosphorylated peptide migrated toward the anode (–). The gel was photographed on a transilluminator, and active free PKA (–cAMP), compared with total PKA (+cAMP), was determined by analyzing phosphorylated bands using ImageJ software (http://rsbweb.nih.gov/ij/).

TRACP 5b ELISA. TRACP 5b was measured in mouse serum using a solid-phase immunofixed enzyme activity assay (MouseTRAP; Immuno Diagnostic Systems). Briefly, mouse blood serum, TRACP 5b standards, and controls were incubated with a polyclonal antibody against mouse TRACP 5b bound to anti-rabbit IgG-coated microtiter wells. After washing, bound TRACP 5b activity was determined with a chromogenic substrate, and the absorbance of the reaction was determined using a microplate reader measuring at 405 nm.

TRAP histochemical staining. Four percent paraformaldehyde or ten percent formalin-fixed bone tissues were decalcified with Immunocal (Decal Chemical Corp.), sectioned at 5 μm, and stained using the Leukocyte Acid Phosphatase (TRAP) kit (Sigma-Aldrich).

Statistics. Details on aCGH and gene expression data analyses are provided in Supplemental Methods. Survival analysis was conducted using the log-rank test. For relating molecular data to the clinical phenotype, Fisher's exact test was used. For integrative gene copy number/expression analysis, Spearman's rank correlation was used. Differential gene expression signatures were generated using Welsh's *t* test, and the Benjamini and Hochberg approach for control of FDR was adopted for gene-wise multiple testing adjustments. Statistical criteria for identification of differentially expressed genes were FDR-adjusted *P* values of less than 0.05, and for other tests a *P* value of less than 0.05 was considered significant. Gene enrichment was examined using the hypergeometric test or EASE analysis.

Acknowledgments

This work was supported by grants from Canadian Institutes of Health Research (no. Mop-64265) and National Cancer Institute of Canada (no. 18122) to R. Khokha and an NIH grant to T.J. Triche. The authors thank Paul Boutros (Ontario Institute for Cancer Research) and Da-Wei Huang (NIH) for discussions on bioinformatic analyses, Kristina Neuman for illustrations, and Paul Waterhouse for critique of the manuscript.

Received for publication January 20, 2010, and accepted in revised form June 30, 2010.

Address correspondence to: Rama Khokha, Princess Margaret Hospital, 610 University Ave., Toronto, Ontario, M5G 2M9, Canada. Phone: 416.946.2051; Fax: 416.246.2984; E-mail: rkhokha@uhnres.utoronto.ca.

1. Zuber J, et al. Mouse models of human AML accurately predict chemotherapy response. *Genes Dev*. 2009;23(7):877–889.
2. Salvesen HB, et al. Integrated genomic profiling of endometrial carcinoma associates aggressive tumors with indicators of PI3 kinase activation. *Proc Natl Acad Sci U S A*. 2009;106(12):4834–4839.
3. Setlur SR, et al. Estrogen-dependent signaling in a molecularly distinct subclass of aggressive prostate cancer. *J Natl Cancer Inst*. 2008;100(11):815–825.
4. Jones S, et al. Core signaling pathways in human pancreatic cancers revealed by global genomic analyses. *Science*. 2008;321(5897):1801–1806.
5. Parsons DW, et al. An integrated genomic analysis of human glioblastoma multiforme. *Science*. 2008;321(5897):1807–1812.
6. Forbes SA, et al. The Catalogue of Somatic Mutations in Cancer (COSMIC). *Curr Protoc Hum Genet*. 2010;Chapter 10:Unit 10.11.
7. Wood LD, et al. The genomic landscapes of human breast and colorectal cancers. *Science*. 2007; 318(5853):1108–1113.
8. Maser RS, et al. Chromosomally unstable mouse tumours have genomic alterations similar to diverse human cancers. *Nature*. 2007;447(7147):966–971.
9. Herschkowitz JI, et al. Identification of conserved gene expression features between murine mammary carcinoma models and human breast tumors. *Genome Biol*. 2007;8(5):R76.
10. Sweet-Cordero A, et al. An oncogenic KRAS2 expression signature identified by cross-species gene-expression analysis. *Nat Genet*. 2005;37(1):48–55.
11. Kim M, et al. Comparative oncogenomics identifies NEDD9 as a melanoma metastasis gene. *Cell*. 2006;125(7):1269–1281.
12. Zender L, et al. Identification and validation of oncogenes in liver cancer using an integrative oncogenomic approach. *Cell*. 2006;125(7):1253–1267.
13. Clark JC, Dass CR, Choong PF. A review of clinical and molecular prognostic factors in osteosarcoma. *J Cancer Res Clin Oncol*. 2008;134(3):281–297.
14. Link MP, Gebhardt MC, Meyers PA. Osteosarcoma. In: Pizzo PA, Poplack DG, eds. *Principles and Practice of Pediatric Oncology*. 5th ed. Philadelphia, Pennsylvania, USA: Lippincott Williams and Wilkins; 2005:1074–1115.
15. Lau CC, et al. Frequent amplification and rearrangement of chromosomal bands 6p12-p21 and 17p11.2 in osteosarcoma. *Genes Chromosomes Cancer*. 2004;39(1):11–21.
16. Fuchs B, Pritchard DJ. Etiology of osteosarcoma. *Clin Orthop Relat Res*. 2002;(397):40–52.
17. Patino-Garcia A, Pineiro ES, Diez MZ, Iturriagagoitia LG, Klussmann FA, Ariznabarreta LS. Genetic and epigenetic alterations of the cell cycle regulators and tumor suppressor genes in pediatric osteosarcomas. *J Pediatr Hematol Oncol*. 2003;25(5):362–367.
18. Ladanyi M, Cha C, Lewis R, Jhanwar SC, Huvos AG, Healey JH. MDM2 gene amplification in metastatic osteosarcoma. *Cancer Res*. 1993;53(1):16–18.
19. Wei G, et al. CDK4 gene amplification in osteosarcoma: reciprocal relationship with INK4A gene alterations and mapping of 12q13 amplicons. *Int J Cancer*. 1999;80(2):199–204.
20. Walkley CR, et al. Conditional mouse osteosarcoma, dependent on p53 loss and potentiated by loss of Rb, mimics the human disease. *Genes Dev*. 2008;22(12):1662–1676.
21. Berman SD, et al. Metastatic osteosarcoma induced by inactivation of Rb and p53 in the osteoblast lineage. *Proc Natl Acad Sci U S A*. 2008;105(33):11851–11856.
22. Lin PP, Pandey MK, Jin F, Raymond AK, Akiyama H, Lozano G. Targeted mutation of p53 and Rb in mesenchymal cells of the limb bud produces sarcomas in mice. *Carcinogenesis*. 2009; 30(10):1789–1795.
23. Ferracini R, et al. The Met/HGF receptor is overexpressed in human osteosarcomas and is activated by either a paracrine or an autocrine circuit. *Oncogene*. 1995;10(4):739–749.
24. Ladanyi M, Park CK, Lewis R, Jhanwar SC, Healey JH, Huvos AG. Sporadic amplification of the MYC gene in human osteosarcomas. *Diagn Mol Pathol*. 1993;2(3):163–167.
25. Weisstein JS, Majeska RJ, Klein MJ, Einhorn TA. Detection of c-fos expression in benign and malignant musculoskeletal lesions. *J Orthop Res*. 2001;19(3):339–345.
26. Ruther U, Komitowski D, Schubert FR, Wagner EF. c-fos expression induces bone tumors in transgenic mice. *Oncogene*. 1989;4(7):861–865.
27. Frendo JL, Xiao G, Fuchs S, Franceschi RT, Karsenty G, Ducy P. Functional hierarchy between two OSE2 elements in the control of osteocalcin gene expression in vivo. *J Biol Chem*. 1998;273(46):30509–30516.
28. Ahuja D, Saenz-Robles MT, Pipas JM. SV40 large T antigen targets multiple cellular pathways to elicit cellular transformation. *Oncogene*. 2005; 24(52):7729–7745.
29. Chen W, Possemato R, Campbell KT, Plattner CA, Pallas DC, Hahn WC. Identification of specific PP2A complexes involved in human cell transformation. *Cancer Cell*. 2004;5(2):127–136.
30. Luo X, et al. Osteogenic BMPs promote tumor growth of human osteosarcomas that harbor differentiation defects. *Lab Invest*. 2008;88(12):1264–1277.
31. Kim C, Cheng CY, Saldanha SA, Taylor SS. PKA-I holoenzyme structure reveals a mechanism for cAMP-dependent activation. *Cell*. 2007; 130(6):1032–1043.
32. Swarthout JT, D'Alonzo RC, Selvamurugan N, Partridge NC. Parathyroid hormone-dependent signaling pathways regulating genes in bone cells. *Gene*. 2002;282(1–2):1–17.
33. Barger AM, Fan TM, de Lorimier LP, Sprandel IT, O'Dell-Anderson K. Expression of receptor activator of nuclear factor kappa-B ligand (RANKL) in neoplasms of dogs and cats. *J Vet Intern Med*. 2007;21(1):133–140.
34. Lamoureux F, et al. Glycosaminoglycans as potential regulators of osteoprotegerin therapeutic activity in osteosarcoma. *Cancer Res*. 2009;69(2):526–536.
35. Lamoureux F, et al. Therapeutic relevance of osteoprotegerin gene therapy in osteosarcoma: blockade of the vicious cycle between tumor cell proliferation and bone resorption. *Cancer Res*. 2007;67(15):7308–7318.
36. Jones DH, et al. Regulation of cancer cell migration and bone metastasis by RANKL. *Nature*. 2006;440(7084):692–696.
37. Yang D, Singh R, Divieti P, Guo J, Bouxsein ML, Bringhurst FR. Contributions of parathyroid hormone (PTH)/PTH-related peptide receptor signaling pathways to the anabolic effect of PTH on bone. *Bone*. 2007;40(6):1453–1461.
38. Fu Q, Jilka RL, Manolagas SC, O'Brien CA. Parathyroid hormone stimulates receptor activator of NFkappa B ligand and inhibits osteoprotegerin expression via protein kinase A activation of cAMP-response element-binding protein. *J Biol Chem*. 2002;277(50):48868–48875.
39. Kirschner LS, et al. A mouse model for the Carney complex tumor syndrome develops neoplasia in cyclic AMP-responsive tissues. *Cancer Res*. 2005;65(11):4506–4514.
40. Dacquin R, Starbuck M, Schinke T, Karsenty G. Mouse alpha1(I)-collagen promoter is the best known promoter to drive efficient Cre recombinase expres-

sion in osteoblast. *Dev Dyn*. 2002;224(2):245–251.
41. Grimaud E, et al. Receptor activator of nuclear factor kappaB ligand (RANKL)/osteoprotegerin (OPG) ratio is increased in severe osteolysis. *Am J Pathol*. 2003;163(5):2021–2031.
42. Pavel E, Nadella K, Towns WH 2nd, Kirschner LS. Mutation of Prkar1a causes osteoblast neoplasia driven by dysregulation of protein kinase A. *Mol Endocrinol*. 2008;22(2):430–440.
43. Paoloni M, et al. Canine tumor cross-species genomics uncovers targets linked to osteosarcoma progression. *BMC Genomics*. 2009;10:625.
44. Mak KK, et al. Hedgehog signaling in mature osteoblasts regulates bone formation and resorption by controlling PTHrP and RANKL expression. *Dev Cell*. 2008;14(5):674–688.
45. Kansara M, et al. Wnt inhibitory factor 1 is epigenetically silenced in human osteosarcoma, and targeted disruption accelerates osteosarcomagenesis in mice. *J Clin Invest*. 2009;119(4):837–851.
46. Bossis I, Stratakis CA. Minireview: PRKAR1A: normal and abnormal functions. *Endocrinology*. 2004;145(12):5452–5458.
47. Bossis I, Voutetakis A, Bei T, Sandrini F, Griffin KJ, Stratakis CA. Protein kinase A and its role in human neoplasia: the Carney complex paradigm. *Endocr Relat Cancer*. 2004;11(2):265–280.
48. Tsang KM, et al. Alternate protein kinase A activity identifies a unique population of stromal cells in adult bone. *Proc Natl Acad Sci U S A*. 2010; 107(19):8683–8688.
49. Kirschner LS, et al. Mutations of the gene encoding the protein kinase A type I-alpha regulatory subunit in patients with the Carney complex. *Nat Genet*. 2000;26(1):89–92.
50. Carney JA, et al. Osteochondromyxoma of bone: a congenital tumor associated with lentigines and other unusual disorders. *Am J Surg Pathol*. 2001;25(2):164–176.
51. Almeida MQ, et al. Mouse Prkar1a haploinsufficiency leads to an increase in tumors in the $Trp53^{+/-}$ or $Rb1^{+/-}$ backgrounds and chemically induced skin papillomas by dysregulation of the cell cycle and Wnt signaling. *Hum Mol Genet*. 2010; 19(8):1387–1398.
52. Scotlandi K, et al. Clinical relevance of Ki-67 expression in bone tumors. *Cancer*. 1995;75(3):806–814.
53. Weinstein LS, Liu J, Sakamoto A, Xie T, Chen M. Minireview: GNAS: normal and abnormal functions. *Endocrinology*. 2004;145(12):5459–5464.
54. Doganavsargil B, Argin M, Kececi B, Sezak M, Sanli UA, Oztop F. Secondary osteosarcoma arising in fibrous dysplasia, case report. *Arch Orthop Trauma Surg*. 2009;129(4):439–444.
55. Jhala DN, et al. Osteosarcoma in a patient with McCune-Albright syndrome and Mazabraud's syndrome: a case report emphasizing the cytological and cytogenetic findings. *Hum Pathol*. 2003; 34(12):1354–1357.
56. Walsh MC, et al. Osteoimmunology: interplay between the immune system and bone metabolism. *Annu Rev Immunol*. 2006;24:33–63.
57. Kong YY, et al. OPGL is a key regulator of osteoclastogenesis, lymphocyte development and lymph-node organogenesis. *Nature*. 1999;397(6717):315–323.
58. Mori K, et al. Human osteosarcoma cells express functional receptor activator of nuclear factor-kappa B. *J Pathol*. 2007;211(5):555–562.
59. Onyia JE, et al. Molecular profile of catabolic versus anabolic treatment regimens of parathyroid hormone (PTH) in rat bone: an analysis by DNA microarray. *J Cell Biochem*. 2005;95(2):403–418.
60. Klein MJ, Siegal GP. Osteosarcoma: anatomic and histologic variants. *Am J Clin Pathol*. 2006;125(4):555–581.
61. Kearns AE, Khosla S, Kostenuik PJ. Receptor activator of nuclear factor kappaB ligand and osteoprotegerin regulation of bone remodeling in health and disease. *Endocr Rev*. 2008;29(2):155–192.
62. Mori S, et al. Utilization of pathway signatures to reveal distinct types of B lymphoma in the Emicromyc model and human diffuse large B-cell lymphoma. *Cancer Res*. 2008;68(20):8525–8534.
63. Osborne LR, Joseph-George AM, Scherer SW. Williams-Beuren syndrome diagnosis using fluorescence in situ hybridization. *Methods Mol Med*. 2006;126:113–128.
64. Arndt CA, Crist WM. Common musculoskeletal tumors of childhood and adolescence. *N Engl J Med*. 1999;341(5):342–352.
65. Unni KK, ed. *Dahlin's Bone Tumors: General Aspects And Data On 11,080 Cases*. 5th ed. Philadelphia, Pennsylvania, USA: Lippencott-Raven; 1996.